Tectonics®

RESEARCH ARTICLE
10.1029/2024TC008415

One Billion Years of Stability in the North American Midcontinent Following Two-Stage Grenvillian Structural Inversion

Eben B. Hodgin[1,2], Nicholas L. Swanson-Hysell[2], Andrew R. C. Kylander-Clark[3], Andrew C. Turner[2,4], Daniel A. Stolper[2], Daniel E. Ibarra[1], Mark D. Schmitz[5], Yiming Zhang[2], Luke M. Fairchild[2], and Anthony J. Fuentes[2]

[1]Department of Earth, Environmental, and Planetary Science, Brown University, Providence, RI, USA, [2]Department of Earth and Planetary Science, University of California, Berkeley, Berkeley, CA, USA, [3]Department of Earth Science, University of California, Santa Barbara, Santa Barbara, CA, USA, [4]Now at Central Energy Resources Science Center, U.S. Geological Survey, Denver, CO, USA, [5]Department of Geosciences, Boise State University, Boise, ID, USA

Abstract The North American craton interior preserves a >1 Ga history of near surface processes that inform ongoing debates regarding timing and drivers of continental-scale deformation and erosion associated with far-field orogenesis. We tested various models of structural inversion on a major segment of the Midcontinent Rift along the Douglas Fault in northern Wisconsin, which accommodated ≳10 km of total vertical displacement. U-Pb detrital zircon and vein calcite Δ_{47}/U-Pb thermochronometry from the hanging wall constrain the majority of uplift (≳8.5 km) and deformation to 1052–1036 Ma during the Ottawan phase of the Grenvillian orogeny. Combined U-Pb zircon dates, Δ_{47}/U-Pb calcite thermochronometry, and field data that document syn- to early post-depositional deformation in the footwall constrain a second stage of uplift (1–1.5 km) ca. 995–980 Ma during the Rigolet phase of the Grenvillian orogeny. A minor phase of Appalachian far-field orogenesis is associated with minimal thrust reactivation. Our combined analyses identified the 995–980 Ma Bayfield Group as a Grenvillian foreland basin with an original thickness 0.5–2 km greater than currently preserved. By quantifying flexural loading and other subsidence mechanisms along the Douglas Fault, we identify dynamic subsidence as a mechanism that could be consistent with the development of late-Grenvillian transcontinental fluvial systems. Minimal post-Grenvillian erosion (0.5–2 km) in this part of the craton interior has preserved the Bayfield Group and equivalent successions, limiting the magnitude of regional erosion that can be attributed to Neoproterozoic glaciation.

Plain Language Summary Around 1.1 billion years ago, volcanic rocks and sediments began accumulating in a large rift basin around the present-day Lake Superior region of North America. Continent-continent collision on the edge of North America caused rifting to cease and major uplift to occur on thrust faults in the rift. The timing of the tectonic shift and the amount of crustal uplift and the number of uplift episodes are all poorly constrained. Our new geochronology precisely identifies the age of two major uplift episodes, ~1.05 and ~0.98 billion years ago. Mineral veins that formed during uplift record the age and temperature of formation, which enables reconstruction of an uplift history. We conclude that the collisional event ~1.05 billion years ago resulted in ≳8.5 km of uplift followed by 1.0–1.5 km of uplift ~0.98 billion years ago. A sedimentary basin associated with collision ~1.0 billion years ago may have been part of a vast transcontinental river system. The surface underlying the Great Unconformity, a surface representing missing time, regionally did not undergo much erosion following uplift, suggesting long-term stability of the North American craton interior over the last ~0.98 billion years.

Key Points:

- U-Pb zircon and calcite dates constrain two-stage Grenvillian inversion of the Midcontinent Rift on the Douglas Fault in northern Wisconsin
- Δ_{47}/U-Pb thermochronometry constrains vertical displacement of ≳8.5 and ~1.5 km in the Ottawan and Rigolet Grenvillian phases, respectively
- Basin analysis and clay mineralogy constrain original thickness, subsidence drivers, and erosion of a ca. 1010–980 Ma Grenvillian foreland

Supporting Information:

Supporting Information may be found in the online version of this article.

Correspondence to:

E. B. Hodgin,
eben_hodgin@brown.edu

Citation:

Hodgin, E. B., Swanson-Hysell, N. L., Kylander-Clark, A. R. C., Turner, A. C., Stolper, D. A., Ibarra, D. E., et al. (2024). One billion years of stability in the North American Midcontinent following two-stage Grenvillian structural inversion. *Tectonics*, *43*, e2024TC008415. https://doi.org/10.1029/2024TC008415

Received 14 MAY 2024
Accepted 26 AUG 2024
Corrected 5 NOV 2024

This article was corrected on 5 NOV 2024. See the end of the full text for details.

Author Contributions:

Conceptualization: Eben B. Hodgin
Data curation: Nicholas L. Swanson-Hysell, Andrew C. Turner, Daniel A. Stolper, Daniel E. Ibarra, Mark D. Schmitz
Formal analysis: Eben B. Hodgin, Andrew R. C. Kylander-Clark, Andrew C. Turner, Daniel A. Stolper, Daniel E. Ibarra, Mark D. Schmitz
Funding acquisition: Nicholas L. Swanson-Hysell

1. Introduction

It has been shown that compression due to the collision of tectonic plates can be transmitted over great distances through continental lithosphere, resulting in the reactivation of pre-existing crustal discontinuities, thrusting of basement blocks, and inversion of extensional basins (Cannon, 1994; Horton et al., 2022; Ziegler et al., 1995). The geological record of cratonic interiors, which have generally been subjected to less deformation and erosion than continental margins, can thus preserve tectonic and Earth history events that may be poorly preserved on continental margins. The late Mesoproterozoic Midcontinent Rift within the Laurentian craton of North America is a major tectono-magmatic feature that underwent crustal-scale structural inversion following extension

Investigation: Eben B. Hodgin, Nicholas L. Swanson-Hysell, Andrew C. Turner, Daniel E. Ibarra, Mark D. Schmitz, Yiming Zhang, Luke M. Fairchild, Anthony J. Fuentes
Methodology: Eben B. Hodgin, Andrew R. C. Kylander-Clark, Andrew C. Turner, Daniel A. Stolper, Daniel E. Ibarra, Mark D. Schmitz
Project administration: Nicholas L. Swanson-Hysell
Resources: Nicholas L. Swanson-Hysell, Andrew R. C. Kylander-Clark, Daniel A. Stolper, Daniel E. Ibarra, Mark D. Schmitz, Luke M. Fairchild
Software: Mark D. Schmitz
Supervision: Nicholas L. Swanson-Hysell
Validation: Nicholas L. Swanson-Hysell, Daniel A. Stolper, Daniel E. Ibarra, Mark D. Schmitz
Visualization: Eben B. Hodgin, Nicholas L. Swanson-Hysell, Yiming Zhang
Writing – original draft: Eben B. Hodgin
Writing – review & editing: Eben B. Hodgin, Nicholas L. Swanson-Hysell, Andrew C. Turner, Daniel A. Stolper, Daniel E. Ibarra, Yiming Zhang, Anthony J. Fuentes

(Cannon et al., 1993). The inverted strata, which occur in a belt that extends >2,000 km from southern Ontario to Kansas, consist of >10 km of rift-related volcanic and sedimentary rocks (Figure 1; Chandler et al., 1989; Ojakangas et al., 2001; Van Schmus and Hinze, 1985). The timing of eruptions and deposition coincided with an interval of rapid plate motion (20–30 cm/year: Swanson-Hysell et al., 2019) prior to the Himalayan-scale Grenvillian Orogeny on the eastern margin of Laurentia (Hynes and Rivers, 2010). It has been proposed that far-field effects of the 1090 to 980 Ma Grenvillian orogeny (Swanson-Hysell et al., 2023) caused cessation of extension and subsequent crustal-scale inversion in the Midcontinent Rift (Cannon, 1994; Cannon et al., 1993). However, sparse age constraints on the timing of inversion have contributed to a range of tectonic interpretations, including single-stage Grenvillian inversion (Cannon, 1994; Swanson-Hysell et al., 2019), two-stage Grenvillian inversion (Hodgin, Swanson-Hysell, et al., 2022), and post-Grenvillian inversion (Craddock et al., 2017).

To test regional synchroneity in the timing of inversion and to quantify the amount of uplift associated with shortening during distinct episodes of far-field orogenesis, we investigated a segment of the Midcontinent Rift along the Douglas Fault in northern Wisconsin and relevant nearby sites (Figures 1 and 2). In addition to shedding light on the geodynamic evolution of the Midcontinent Rift system, paired U-Pb geochronology and clumped isotope thermometry on fault-associated vein calcite can place constraints on the uplift and erosion history of the midcontinent. Low-temperature thermochronology and basin analysis from the craton interior in northern Wisconsin—that we compare to similar compiled data sets from Minnesota, Wisconsin, and Michigan—are well-suited to document its prolonged stability and to differentiate between opposing hypotheses associated with the timing and amount of erosion in the continental interior.

2. Geologic Setting

The Douglas Fault in northern Wisconsin and eastern Minnesota is one of the major faults that accommodated structural inversion of the Midcontinent Rift (Figures 1 and 2). Similar to other regional reverse faults, the Douglas Fault thrusts ca. 1100–1090 Ma rift-related volcanic rocks and overlying ca. 1090–1050 Ma rift-related sedimentary rocks of the Oronto Group atop younger post-rift sandstones (Figure 2; van Schmus and Hinze, 1985). Sedimentary rocks of the post-rift Bayfield Group are folded in the footwall of the Douglas Fault. They are part of a continuous sedimentary belt from northern Wisconsin to eastern Minnesota, where they are referred to as the Fond du Lac and Hinckley formations (Figure 1; Morey and Ojakangas, 1982). The Bayfield Group has been correlated with the lithologically similar Jacobsville Formation (van Schmus and Hinze, 1985), which is folded in the footwall of the Keweenaw and Marenisco thrust faults in northern Michigan, where drag-folding has been linked to a final pulse of contractional deformation during the Rigolet phase of the Grenvillian orogeny (Hodgin, Swanson-Hysell, et al., 2022). While correlation with the Jacobsville Formation would constrain the age of the Bayfield Group to ca. 990 Ma, its age remains uncertain (Craddock et al., 2013) which leads to ambiguity on the timing of final inversion and the subsequent erosional history.

2.1. Regional Stratigraphy

The volcanic succession in the hanging wall of the Douglas Fault was divided by Nicholson et al. (2006) into >10 km of basal Chengwatana Volcanics overlain by 3–5 km of Minong Volcanics with both being constituents of the St. Croix Group (Figure 2). The Minong Volcanics consist of low-Ti basalts and minor rhyolites (Nicholson et al., 2006), including the Nelson Lake Rhyolite dated at 1094.6 ± 2.1 Ma (upper concordia intercept U-Pb zircon date; 2σ analytical uncertainty; Zartman et al., 1997). The ca. 1100 Ma Powder Mill Group in northeastern Wisconsin (Swanson-Hysell et al., 2019; Zartman et al., 1997) may be equivalent in part to Chengwatana Volcanics in the hanging wall of the Douglas Fault; a rhyolite at the top of the Powder Mill Group has been dated at 1098.24 ± 0.45 Ma ($^{206}Pb/^{238}U$ zircon date; 2σ analytical uncertainty; Swanson-Hysell et al., 2019).

The overlying Oronto Group, which is well-exposed in the Ashland syncline in the central axis of the Midcontinent Rift, consists of Copper Harbor Formation coarse-grained siliciclastics, Nonesuch Formation fine-grained siliciclastics, and Freda Formation fluvial siliciclastics (Figures 1 and 2; Hite, 1968). The Oronto Group has a minimum thickness of ∼4 km along the Montreal River which forms the border between northern Wisconsin and Michigan (Figure 1; Hite, 1968; Slotznick et al., 2024). The basal Oronto Group was deposited conformably above the Chengwatana Volcanics (Chandler et al., 1989), although it can progressively onlap older igneous units along rift flanks (Slotznick et al., 2024; Swanson-Hysell et al., 2019). The presence of interbedded volcanics, such as the ca. 1086 Ma Lake Shore Traps in the Copper Harbor Formation (Davis & Paces, 1990;

10.1029/2024TC008415

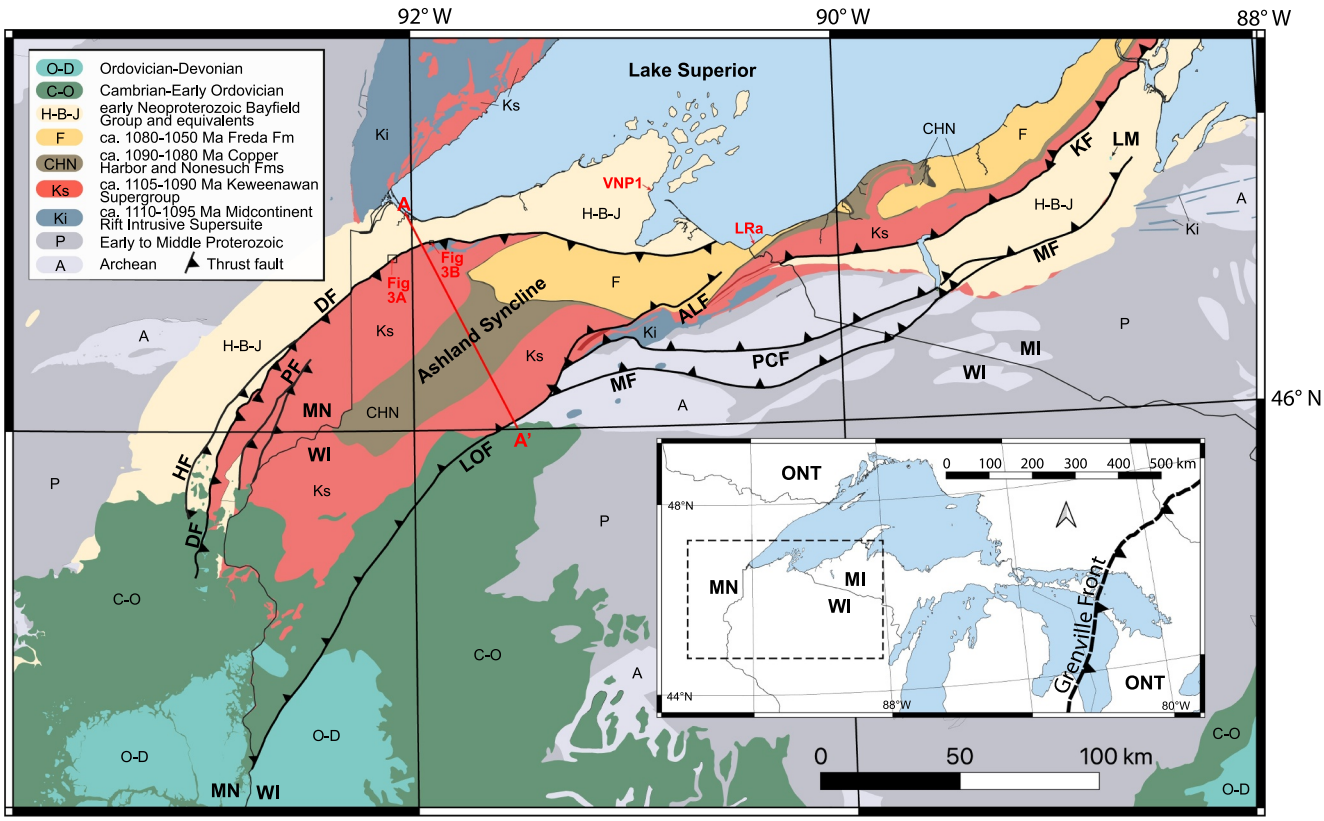

Figure 1. Regional geologic map of the southwestern Lake Superior region with data from Jirsa et al. (2011) and Nicholson et al. (2004). The dashed box in the inset shows the extent of the regional geologic map and location of the Grenville Front relative to the study area. In black: DF, Douglas Fault; HF, Hinckley Fault; PF, Pine Fault; ALF, Atkin's Lake Fault; PCF, Pelton Creek Fault; LOF, Lake Owen Fault; MF, Marenisco Fault; KF, Keweenaw Fault; LM, Limestone Mountain. Cross-section line A-A′ corresponds to Figure 2. The extent of the maps of Figure 3 are shown as well as the location of samples VNP1 and LRa. Global Positioning System locations of samples are provided in Table S1 in Supporting Information S1.

Fairchild et al., 2017) and the Bear Lake Felsite in the Freda Formation (Cannon & Nicholson, 2001), indicate that waning rift-related magmatism persisted during initial Oronto Group deposition (Swanson-Hysell et al., 2019). The Oronto Group has been interpreted as deposited in a thermally subsiding rift basin as active extension waned (Cannon, 1992; Swanson-Hysell et al., 2019). Near the northeastern termination of the Douglas Fault, the Freda Formation is in structural contact with the Bayfield Group (Hite, 1968; Nicholson et al., 2006), which elsewhere is interpreted to overlie the Freda Formation with angular unconformity (Adamson, 1997; Daniels, 1982; Morey and Ojakangas, 1982).

The Bayfield Group is differentiated from the Freda Formation by its more chemically mature quartz-dominated sandstone composition, higher degree of rounding, distinct cements, and distinct clay mineralogy (Adamson, 1997; Myers, 1971; Ojakangas et al., 2001). It has been divided into the Orienta, Devil's Island, and Chequamegon formations (Thwaites, 1912). The Orienta Formation is a feldspathic fluvial sandstone with minor conglomerate and siltstone lithofacies; it has an estimated total thickness of 575 m (Ojakangas et al., 2001). The Devil's Island Formation consists of a mature quartz arenite unit that formed in shallow lacustrine and eolian environments within a braided river system; it has a restricted spatial distribution and an estimated thickness of 90 m (Adamson, 1997; Ojakangas et al., 2001). The Chequamegon Formation is a predominantly fluvial sandstone that is similar lithologically to the Orienta Formation; it contains siltstone interbeds and has an estimated thickness of 150 m (Ojakangas et al., 2001). Due to the lithological similarity of the Orienta and Chequamegon Formations and the Chequamegon Formation being identified primarily on the basis of overlying the spatially limited Devil's Island Formation, it has been proposed that the Chequamegon Formation is equivalent to the upper part of the Orienta Formation (Adamson, 1997). A total estimated thickness of the Bayfield Group is 815 m (Ojakangas et al., 2001). This thickness is similar to an estimate of 750 m and an observed drill core thickness of 656 m from the Fond du Lac

10.1029/2024TC008415

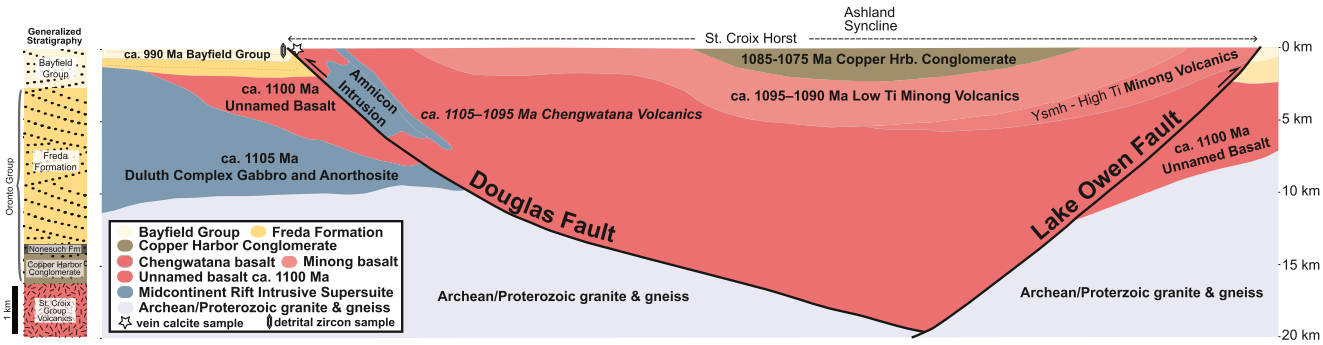

Figure 2. Structural cross-section and stratigraphy of the Midcontinent Rift in northern Wisconsin. The line of cross section (A-A′ on Figure 1) is from Nicholson et al. (2006). The geological units are modified after Nicholson et al. (2006). Unit thicknesses in the Generalized Stratigraphy (left) are based on the Montreal River Monocline (near site LRa in Figure 1).

and Hinckley formations (Morey and Ojakangas, 1982), which together make up the equivalent of the Bayfield Group adjacent to the Douglas Fault in eastern Minnesota (Figure 1). Interpretations of seismic reflection data have suggested that the wedge-shaped basin may be even thicker adjacent to the Douglas Fault (Chandler et al., 1989; Nicholson et al., 2006). Although such estimates could be complicated by the presence of underlying Oronto Group sediments, we consider a maximum present-day Bayfield Group thickness to be ∼1,000 m, which is comparable to the thickest borehole of the correlative Jacobsville Formation (Kalliokoski, 1982; Supporting Information S1).

Midcontinent Rift strata in the northern Wisconsin study area have an estimated total thickness of 20 km (Figure 2; Nicholson et al., 2006) and were subjected to contractional deformation during structural inversion. In contrast, overlying lower Paleozoic sedimentary rocks in the region are generally undeformed (Pinet, 2016; van Schmus and Hinze, 1985), except where minor reactivation of faults (up to a maximum of ∼60 m) has occurred during the middle to late Paleozoic (Setterholm, 2010). The lower Paleozoic strata, which were deposited during Sauk II, Sauk III, and Tippecanoe flooding intervals (Sloss, 1963) consist of upper Cambrian shallow marine sandstone and minor carbonate which is followed by Ordovician shallow marine dolostone/limestone and siliciclastic units (Byers & Dott, 1995; Mossler, 2008). The nearest lower Paleozoic units occur ∼70 km south of the study sites in northern Wisconsin (Figure 1), although mapping of lithofacies migrations on an epeiric ramp (Choi & Simo, 1998; Runkel et al., 2007) has been used to infer a more northerly position of the paleoshoreline prior to subsequent erosion, ∼60 km north of our Pattison and Amnicon Falls state parks study sites (Figures 1 and 3; Eoff, 2014; Lochman-Balk and Holland, 1971). Thin Paleozoic outliers in the region, such as Limestone Mountain in northern Michigan (Figure 1; Milstein, 1987), provide some direct evidence of Paleozoic sedimentation that survived subsequent erosion.

2.2. Regional Structure

The most prominent faults in the Midcontinent Rift are moderate to high-angle reverse faults, which formed along the margins of the central basin (van Schmus and Hinze, 1985). Thrust faults such as the Douglas and Isle Royale faults that occur on the northwestern flank of the Midcontinent Rift dip to the southeast and have opposing vergence to thrust faults that occur on the southeastern flank that dip to the northwest, such as the Lake Owen, Keweenaw, and Marenisco faults (Figure 1). The Douglas Fault has been projected to intersect the Lake Owen Fault at a crustal depth of ∼20 km; together, these two thrust fault systems form a bivergent crustal wedge containing the St. Croix horst and the Ashland syncline (Figure 2; Nicholson et al., 2006). Note that the St. Croix horst is not a horst in the sense of being an elevated region bound by normal faults as in widespread use of the term, but rather an uplifted block bound by reverse faults.

The surface trace of the Douglas Fault forms an arcuate shape that spans >250 km from eastern Minnesota to northeastern Wisconsin (Figure 1; Nicholson et al., 2006). Displacement is greatest near the middle of the fault and less near its southwestern and northeastern terminations (Nicholson et al., 2006). In the middle of the Douglas Fault, near our field sites in northwestern Wisconsin, the zone of fault breccia in the hanging wall can be >100 m wide (Grant, 1901) and total vertical displacement has been estimated as ∼20 km (Figure 2; Nicholson et al., 2006). This amount of displacement is comparable to that on the Marenisco and Pelton Creek faults in the adjacent segment of

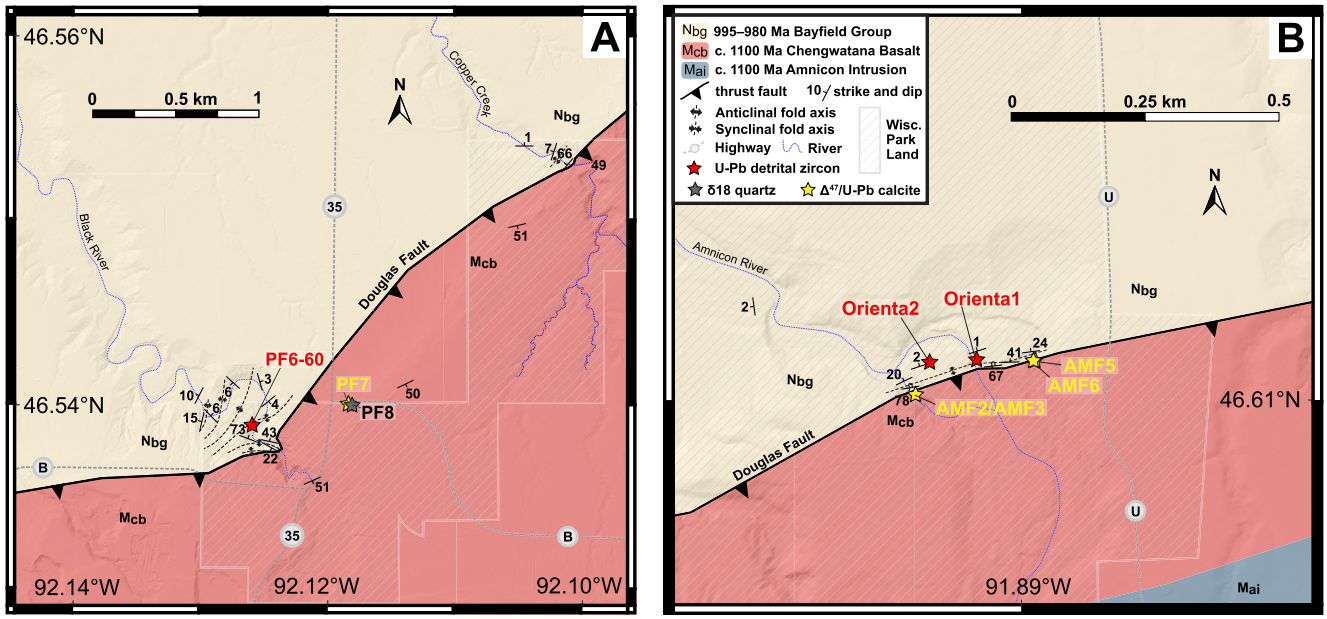

Figure 3. Geological maps of Pattison State Park (a) and Amnicon Falls State Park (b), modified after Nicholson et al. (2006) showing the locations of samples. The extent of each map (which have different scales) is shown in Figure 1. Global Positioning System locations of samples are provided in Table S1 in Supporting Information S1.

the Midcontinent Rift in northern Michigan (Cannon et al., 1993). A more conservative stratigraphic estimate implies ≳10 km of vertical displacement. This estimate is based on the erosional removal of the following units from the hanging wall of the Douglas Fault: ≥4 km of Oronto Group (Slotznick et al., 2024), ∼4 km of Minong Volcanics (Nicholson et al., 2006), and ≥1 km of Chengwatana Volcanics (Nicholson et al., 2006). Additionally, ∼1 km (Ojakangas et al., 2001) of Bayfield Group strata were emplaced in the footwall of the Douglas Fault due to thrust faulting. Taken together, these stratigraphic constraints indicate ≳10 km of total vertical displacement associated with slip on the Douglas Fault.

At Pattison and Amnicon Falls state parks, the Douglas Fault juxtaposes Chengwatana rift-related basalt (Figures 3 and 4) in the hanging wall with post-rift Orienta Formation of the Bayfield Group, which is deformed by fault-propagation and drag folding within the footwall (Figures 2, 3, and 5; Grant, 1901). Farther from its contact with the Douglas Fault (∼10–100 m), strata of the Bayfield Group are generally sub-horizontal (<5° dip; Nicholson et al., 2006).

3. Methods

Field investigation (mapping, sampling, stratigraphic sections, pebble counts) was carried out at sites in northern Wisconsin and northern Michigan. Detrital zircon and vein calcite U-Pb geochronology samples were analyzed at Boise State University and UC Santa Barbara, respectively. Laser ablation–inductively coupled plasma–mass spectrometry (LA-ICP-MS) analyses were used to identify the youngest detrital zircons in each sample (Table S2; Figure S2 in Supporting Information S1), which were then dated by chemical abrasion–isotope dilution–thermal ionization mass spectrometry (CA-ID-TIMS) (Figure 3; Table S3; See Supporting Information S1 for detailed methods). This tandem-dating approach combines the high-throughput, but low-precision, capabilities of LA-ICP-MS with the laborious low-throughput, but high-precision capabilities of CA-ID-TIMS. Tandem-dating is well-suited for the development of accurate and precise maximum depositional ages. Applying CA-ID-TIMS to grains identified as young through LA-ICP-MS mitigates issues from matrix effects, discordance, Pb loss, and low-precision that hamper the interpretation of maximum depositional ages from LA-ICP-MS methods alone (e.g., Herriott et al., 2019; Sharman and Malkowski, 2020). Our approach follows a growing number of studies that have adopted the method of tandem-dating detrital zircons using the youngest single detrital zircon dated by CA-ID-TIMS to establish accurate and precise maximum depositional ages (e.g., Dehler

10.1029/2024TC008415

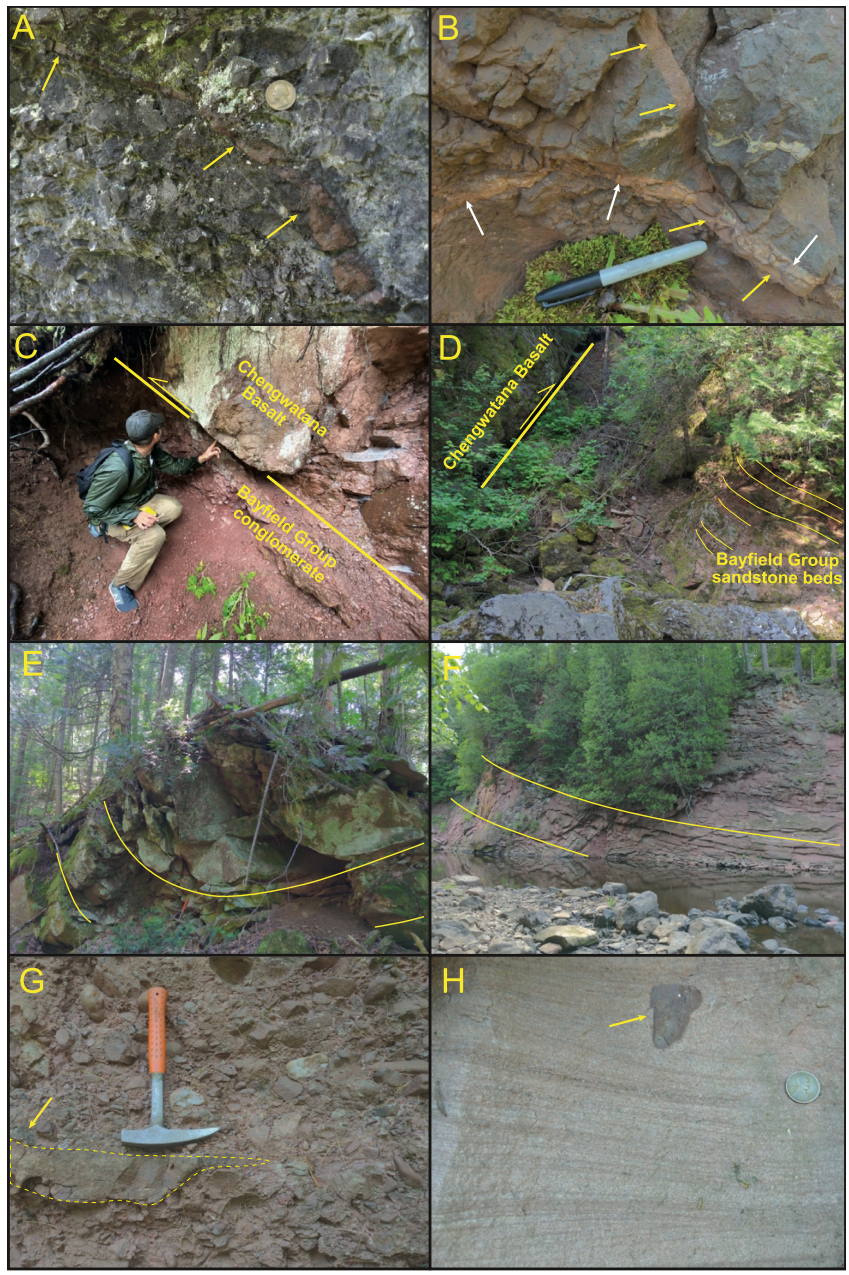

Figure 4. (a, b) Clastic sandstone dikes in the immediate hanging wall of the Douglas Fault at Pattison State Park (a: 46.53725° N; 92.12450° W) (b: 46.54004° N, 92.11802° W). The sandstone dikes have comparable grain size and composition to Bayfield Group sandstone in the footwall. Yellow arrows indicate sandstone dikes crosscutting Chengwatana basalt. In (b), white arrows indicate a quartz vein (sample PF8) crosscut by the sandstone dike. The diameter of the coin in (a) is 2.4 cm and the length of the marker in (b) is 14 cm; (c) The Douglas thrust fault at Amnicon Falls State Park, emplacing ∼1.1 Ga Chengwatana basalt above ∼1.0 Ga Orienta Formation conglomeratic sandstone of the Bayfield Group; (d) The Douglas thrust fault at Copper Creek in Pattison State Park, emplacing ∼1.1 Ga Chengwatana basalt above ∼1.0 Ga Orienta Formation sandstone of the Bayfield Group; (e) An open asymmetric synclinal fold of Bayfield Group sandstone in the immediate footwall of the Douglas Fault at Pattison State Park; (f) The frontal limb of folded Bayfield Group sandstone in the footwall of the Douglas Fault at Pattison State Park; (g) Bayfield Group conglomerate ∼20 m from the Douglas Fault at Pattison State Park. The dashed yellow line delimits a bed of channelized sandstone that occurs within the conglomerate deposits. The yellow arrow indicates a vesicular basalt clast, characteristic of the Chengwatana basalt found in the hanging wall. Pebble counts are presented in Figure 5; (h) Bayfield Group laminated subarkosic arenite ∼50 m from the Douglas Fault at Pattison State Park. The yellow arrow indicates an outsized basalt clast interpreted as derived from the proximal hanging wall.

et al., 2023; Eddy et al., 2016; Gerasimov et al., 2024; Hodgin, Macdonald, et al., 2022; Hodgin, Swanson-Hysell, et al., 2022; Hodgin et al., 2023; Holland et al., 2024; Isakson et al., 2022; Karlstrom et al., 2020; Neil et al., 2021; Perrot et al., 2017; Suarez et al., 2017).

Carbonate clumped isotope measurements of vein calcite were made at UC Berkeley and Brown University to determine the $\delta^{13}C$ and $\delta^{18}O$ and calcite formation temperatures (Δ_{47}; e.g., Ghosh et al., 2006; Huntington & Peterson, 2023). A sufficient number of replicates to determine reliable Δ_{48} measurements and check for kinetic effects was not produced on these samples. We also infer the temperature of formation of associated quartz veins via oxygen isotope measurements by assuming similar source water oxygen isotope compositions from samples of co-located vein calcite (e.g., Abruzzese et al., 2005; Ibarra et al., 2021). 2D flexural modeling of the Bayfield basin adjacent to the St. Croix horst was carried out using Flex2D (Cardozo & Jordan, 2001). Flexural modeling was carried out using Young's modulus and Poisson ratio values of 70 MPa and 0.25, respectively, which are consistent with values typically applied for continental crust, including syn- to post-rift (Burov & Poliakov, 2003) and foreland settings (Garcia-Castellanos & Cloetingh, 2011). Flexural modeling was carried out using an elastic thickness of 30 km, which is consistent with attenuated lithosphere in continental rift basins (Ebinger et al., 1989). The value is also representative of failed rifts with weakened lithospheric strength due to crustal-scale compression (Burov & Diament, 1995; Burov & Poliakov, 2003). See Supporting Information S1 for detailed field methods, U-Pb geochronology methods, carbonate and quartz stable isotope methods, data compilation, and more detailed basin analysis parameters.

4. Results

4.1. Stratigraphic Results

Bayfield Group strata adjacent to the Douglas Fault contain a series of m-thick conglomerate beds interbedded with sandstone that fine upwards (Figure 5). The conglomeratic strata are overlain by trough cross-bedded, medium-grained, subarkosic arenite, containing minor pebbly lenses and pebble lonestones that decrease in abundance up-section. Interbeds of clay-rich red siltstone and silty fine-grained sandstone up to 20 cm thick are more common at Pattison State Park in proximity to the Douglas Fault (Figure S7 in Supporting Information S1). The composition of the conglomerate beds is variable (Figure 5), containing a mixture of clasts derived from the Midcontinent Rift (e.g., basalt, rhyolite, felsite, red fine-grained sandstone likely sourced from the Freda Formation) and from older geological units (e.g., vein quartz and chert). In the AMF section at Amnicon Falls State Park, pebble counts displayed a systematic stratigraphic trend. Basal pebble counts were dominated by volcanics and upper pebble counts were dominated by red fine-grained sandstone (Figure 5). In the PF6 measured section at Pattison State Park, pebble counts were dominated by volcanic clasts and did not show any systematic stratigraphic trend (Figure 5).

4.2. Structural Observations and Results

In the hanging wall of the Douglas Fault at Pattison State Park, Chengwatana basalt and associated calcite and quartz veins are cross-cut by sandstone dikes (Figures 4 and 5), which consist of a moderately well-sorted medium quartz arenite that matches the color, texture, and composition of the Bayfield Group in the immediate footwall. Blocky calcite veins are common in the hanging wall extending up to 50 m from the fault plane; they are typically associated with slickensides, secondary fault planes, and fault gouge. Thin, fibrous vein calcite occurs on the fault plane with fibers oriented perpendicular to the fault plane and inclusion bands of thin clay-rich fault gouge oriented parallel to the fault plane (Figure S8 in Supporting Information S1); these features are consistent with crack-seal emplacement in a tensional stress regime (Ramsay, 1980). The fibrous veins are interpreted as post-dating fault slip and precipitating late within the history of the Douglas Fault.

Relatively simple 10-m scale drag folds of the Bayfield Group occur in the footwall of the Douglas Fault at Copper Creek in Pattison State Park (Figures 3a and 4d) and at Amnicon Falls State Park (Figure 3b). A more complex set of folds with greater amplitude (>10 m) and extending >100 m from the Douglas Fault occur in the Bayfield Group on the Black River at Pattison State Park (Figure 3a); these latter folds are more consistent with fault propagation folds (Suppe and Medwedeff, 1990).

4.3. Zircon U-Pb Geochronology

We collected two sandstone samples from the upper Freda Formation and four sandstone samples from the Bayfield Group for detrital zircon U-Pb geochronology. The Freda Formation samples were collected from

10.1029/2024TC008415

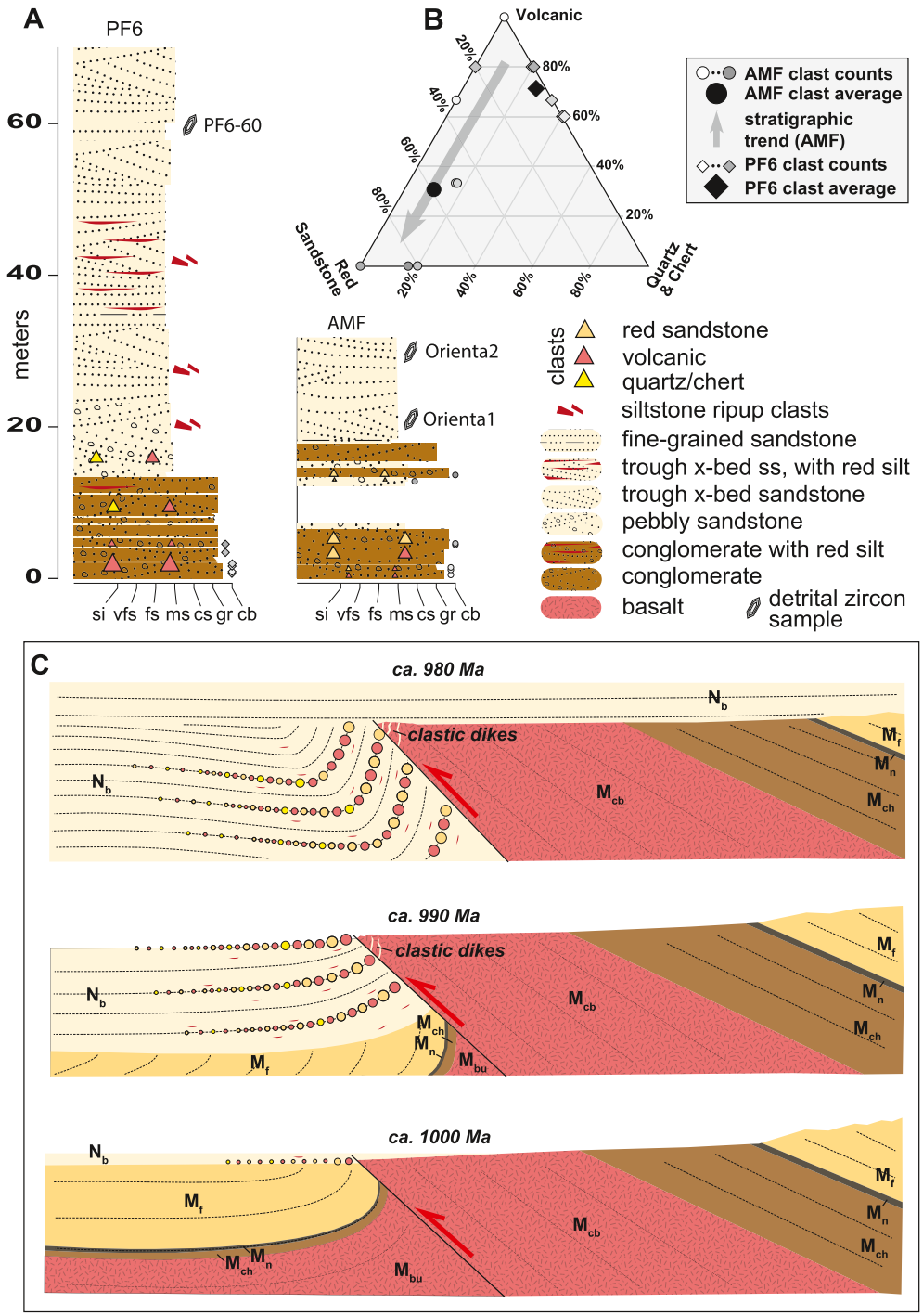

Figure 5. (a) Stratigraphic sections of the Bayfield Group from the footwall of the Douglas Fault at Pattison State Park (PF6) and Amnicon Falls State Park (AMF), WI; (b) Ternary diagram of pebble counts from conglomerates show the percentage of volcanic versus quartz and chert versus red sandstone clasts; (c) A schematic diagram of the evolution of Bayfield Group deposition adjacent to the Douglas Fault and formation of clastic dikes in the hanging wall derived from the Bayfield Group. In a similar tectonic setting, clastic dikes of the correlative Jacobsville Formation have been documented in hanging wall basalts adjacent to the Keweenaw Fault on the Keweenaw Peninsula (Cornwall, 1955). The color of clasts corresponds to the clast lithologies depicted in (a) legend. The depiction of clast size and abundance corresponds to the progressive decrease in clast size and abundance away from the fault. Lithologies follow the stratigraphic column legend above. ss, sandstone; N_b, Neoproterozoic Bayfield Group; M_{bu}, Mesoproterozoic undifferentiated basalt; M_{cb}, Mesoproterozoic Chengwatana basalt; M_{ch}, Mesoproterozoic Copper Harbor Formation; M_n, Mesoproterozoic Nonesuch Formation; M_f, Mesoproterozoic Freda Formation.

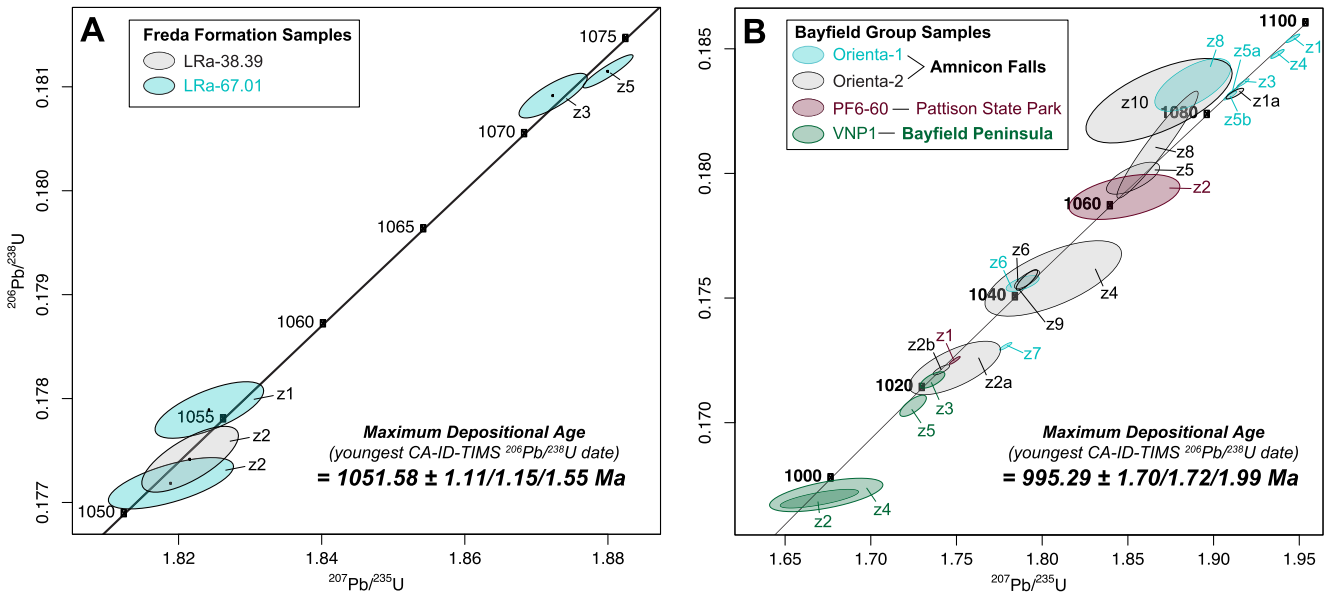

Figure 6. CA-ID-TIMS U-Pb geochronology of detrital zircons from the Freda Formation (a) and Bayfield Group (b). In the Wetherill Concordia plots, analysis numbers (z#) correspond to the color-labeled zircon fractions for each sample. All data including weighted means and modes of the youngest overlapping $^{206}Pb/^{238}U$ dates are reported in Table S3 following the methodology of Nelson et al. (2023). Here, maximum depositional ages are interpreted from the youngest single $^{206}Pb/^{238}U$ date in X/Y/Z format (see Section 3 Methods), where X is the internal error based on analytical uncertainties only, Y includes tracer calibration uncertainty, and Z includes the ^{238}U decay constant uncertainty (Jaffey et al., 1971). CA-ID-TIMS, chemical abrasion–isotope dilution–thermal ionization mass spectrometry.

steeply tilted strata (~80°) near the Michigan-Wisconsin border (LRa in Figure 1) within the southeast limb of the Ashland syncline—also known as the Montreal River Monocline. The samples are located 3.2 km stratigraphically above the base of the >3.4 km-thick Freda Formation and 4.0 km above the base of the Oronto Group (Figure 2 and Figure S1 in Supporting Information S1). The samples come from near the top of a coherent structural panel of Oronto Group strata that is well-exposed along the Montreal River with conformable contacts between the formations of the Oronto Group. These samples thereby constrain the maximum depositional age of the uppermost Oronto Group. In turn, this maximum depositional age establishes the maximum age of the subsequent deformation that tilted the strata during large-scale uplift along the Marenisco Fault. Three sandstone samples of the Bayfield Group were collected from outcrops within the footwall of the Douglas Fault (Figures 1–5). An additional Bayfield Group sample (VNP1) was collected from the Chequamegon Formation at Van Ness Point on the Bayfield Peninsula (Figure 1; Figure S6I in Supporting Information S1).

Following initial screening by LA-ICP-MS to identify young zircon grains (Figure S2 in Supporting Information S1), five zircon grains from the Freda Formation samples (LRa-67.01 and LRa-38.39; Figure S1 in Supporting Information S1) were selected for tandem-dating (see Section 3 Methods) and yielded $^{206}Pb/^{238}U$ CA-ID-TIMS dates ranging from 1072 to 1051 Ma (Table S3). The youngest two CA-ID-TIMS dates are 1052.84 ± 1.42 Ma and 1051.58 ± 1.11 Ma, with the latter defining the maximum depositional age of the upper Freda Formation (Figure 6a). Following screening by LA-ICP-MS (Figure S2 in Supporting Information S1; Table S2), 21 Bayfield Group zircons were selected for U-Pb tandem-dating using CA-ID-TIMS (Figure 6b; Table S3). Two Bayfield Group samples from the footwall of the Douglas Fault at Amnicon Falls (Orienta1 and Orienta2) yielded 15 concordant $^{206}Pb/^{238}U$ CA-ID-TIMS dates ranging from 1096 Ma to 1023 Ma. The site maximum depositional age is determined from a single detrital zircon that was split into two fragments with overlapping $^{206}Pb/^{238}U$ dates with a weighted mean of 1023.79 ± 0.90 Ma (MSWD = 0.03; POF = 0.63; MSWD—Mean Square Weighted Deviation; POF—Probability of Fit) (Figure 6b). One sample from the footwall of the Douglas Fault at Pattison Falls (PF6-60) yielded two CA-ID-TIMS $^{206}Pb/^{238}U$ dates, with the youngest (1025.86 ± 0.69 Ma) representing the maximum depositional age at the site. Sample VNP1 yielded four CA-ID-TIMS $^{206}Pb/^{238}U$ dates ranging from 1022 to 995 Ma. The youngest two dates are 996.11 ± 3.02 Ma and 995.29 ± 1.70 Ma, with the latter defining the maximum depositional age of the Bayfield Group (Figure 6b).

4.4. Calcite U-Pb Geochronology and Clumped-Isotope Thermometry

We collected nine samples of vein calcite for U-Pb LA-ICP-MS geochronology from the Douglas Fault zone at Amnicon Falls State Park (Figure 3b; Figure S8 in Supporting Information S1). Seven samples yielded data dominated by non-radiogenic Pb that could not be used to calculate a lower intercept date. Two samples yielded interpretable isochrons, a thick blocky vein from within the hanging wall fault zone (~3 m from the fault plane: AMF6) and a thin blocky vein (AMF5) within 10 cm of the fault plane, and adjacent to thin, fibrous vein calcite from the fault plane itself (AMF2 and AMF3). Using all data (n = 96/96) from four analyzed calcite crystals, sample AMF6 yielded a lower intercept U-Pb date of 1052 ± 13 Ma (2σ) (Figure S3 in Supporting Information S1; MSWD = 1.1, POF = 0.22, n = 96/96). Each of the four analyzed crystals (1–4) were investigated separately, with crystals 2–4 yielding isochrons with overlapping initial Pb isotopic compositions of 0.868 ± 0.018, 0.875 ± 0.021, and 0.867 ± 0.018; and overlapping lower intercept dates of 1068 ± 24 Ma (2σ), 1060 ± 59 Ma (2σ), and 1039 ± 17 Ma (2σ) (Figure S3 in Supporting Information S1). The lack of appreciable U within crystal 1 precludes it yielding an interpretable isochron. This difference along with slightly elevated initial Pb isotopic composition suggests precipitation from distinct fluids and therefore makes sense to exclude from the combined isochron. The data from crystals 2–4 (n = 77/96) yielded an isochron of 1049 ± 13 Ma (2σ) (Figure 7; MSWD = 0.98, POF = 0.53). In comparison with the isochron using all data, this latter isochron from crystals 2–4 is also preferred on account of having a significantly improved POF. Sample AMF5 yielded a lower intercept date of 298.5 ± 50.3 Ma (2σ, MSWD = 1.3, POF = 0.05, n = 88/99) (Figure 7).

Both samples that yielded isochron dates (AMF5 and AMF6), plus two samples from late-stage, thin, fibrous vein calcite (AMF2 and AMF3), were subsequently analyzed for carbonate clumped isotopes and $\delta^{13}C$ and $\delta^{18}O$ values (relative to the VPDB scale). Two calcite vein samples (PF2 and PF7), adjacent to quartz vein PF8 at Pattison State Park (Figures 3 and 4), were also analyzed for clumped isotopes and $\delta^{13}C$ and $\delta^{18}O$. The combined Δ_{47}-based temperature from three separate crystals of AMF6 is 54.4 ± 1.7°C and the $\delta^{13}C$ and $\delta^{18}O$ values are −0.66‰ and −12.09‰, respectively (1 s.e.; Figure 1; Table S5). The Δ_{47}-based temperature of AMF5 is 33.0°C and the $\delta^{13}C$ and $\delta^{18}O$ values are −4.97‰ and −7.50‰, respectively. The combined Δ_{47}-based temperature of AMF2 and AMF3 is 38.3 ± 2.2°C and the combined mean $\delta^{13}C$ and $\delta^{18}O$ values are −9.1‰ and −6.4‰, respectively. The Δ_{47}-based temperatures of PF2 and PF7 are 56.9 ± 4.6°C and 67.6 ± 1.1°C, respectively. The $\delta^{13}C$ and $\delta^{18}O$ values of PF2 are −2.2‰ and −11.1‰. The $\delta^{13}C$ and $\delta^{18}O$ values of PF7 are −3.1‰ and −10.8‰. The $\delta^{18}O$ values of PF8 quartz is 16.81 ± 0.28‰ (2σ; VSMOW; Vienna Standard Mean Ocean Water). This value equates to a temperature estimate between 130 and 113°C by combining the carbonate-water equilibrium fractionation factor (Jautzy et al., 2020) to derive the source water $\delta^{18}O$ from the two most closely associated calcite veins, PF2 and PF7, using the silica-water equilibrium fractionation factor of Sharp et al. (2016). The assumption of source water $\delta^{18}O$ from the calcite that likely formed at a later time introduces uncertainty into this estimate, but provides the only constraint we have available. This temperature range is consistent with those estimated for the formation of laumontite veins (150 ± 25°C; Bodden et al., 2022) which are located in the same fracture plane as the quartz vein.

Vein calcite sample data from the Douglas Fault were compared to U-Pb and clumped isotope data from two vein calcite samples from the Keweenaw Fault zone in northern Michigan (LLB6 and GRL2 [Figure 7; Figures S4–S6 in Supporting Information S1]). GRL2 yielded a date of 1052 ± 36 Ma and a Δ_{47}-based temperature of 60.8 ± 3.6°C. LLB6 yielded two distinct arrays of U-Pb data that can be captured by two separate isochron dates of 1048 ± 87 Ma and 378 ± 150 Ma (Figure S4 in Supporting Information S1). LLB6 has a corresponding Δ_{47}-based temperature of 44.7 ± 1.9°C. All isotopic data is reported in Supporting Information S1 (Table S5).

5. Discussion

The structural inversion of the Midcontinent Rift resulted in the re-cratonization of the North American interior. An outstanding question is whether structural inversion occurred during the Ottawan and/or Rigolet phase of the Grenvillian orogeny (Cannon, 1994; Hodgin, Swanson-Hysell, et al., 2022; Swanson-Hysell et al., 2019) and/or during post-Grenvillian orogenesis (Craddock et al., 2017). New constraints on the timing of Midcontinent Rift inversion can thus be used to link episodes of orogenesis on the margin of Laurentia to the uplift and erosional history of the continental interior. From the constraints developed in this study, we put forward a framework for the timing and magnitude of slip during three distinct intervals of shortening on the Douglas Fault that inform the geodynamic evolution of the Midcontinent Rift and are followed by a discussion of broader implications,

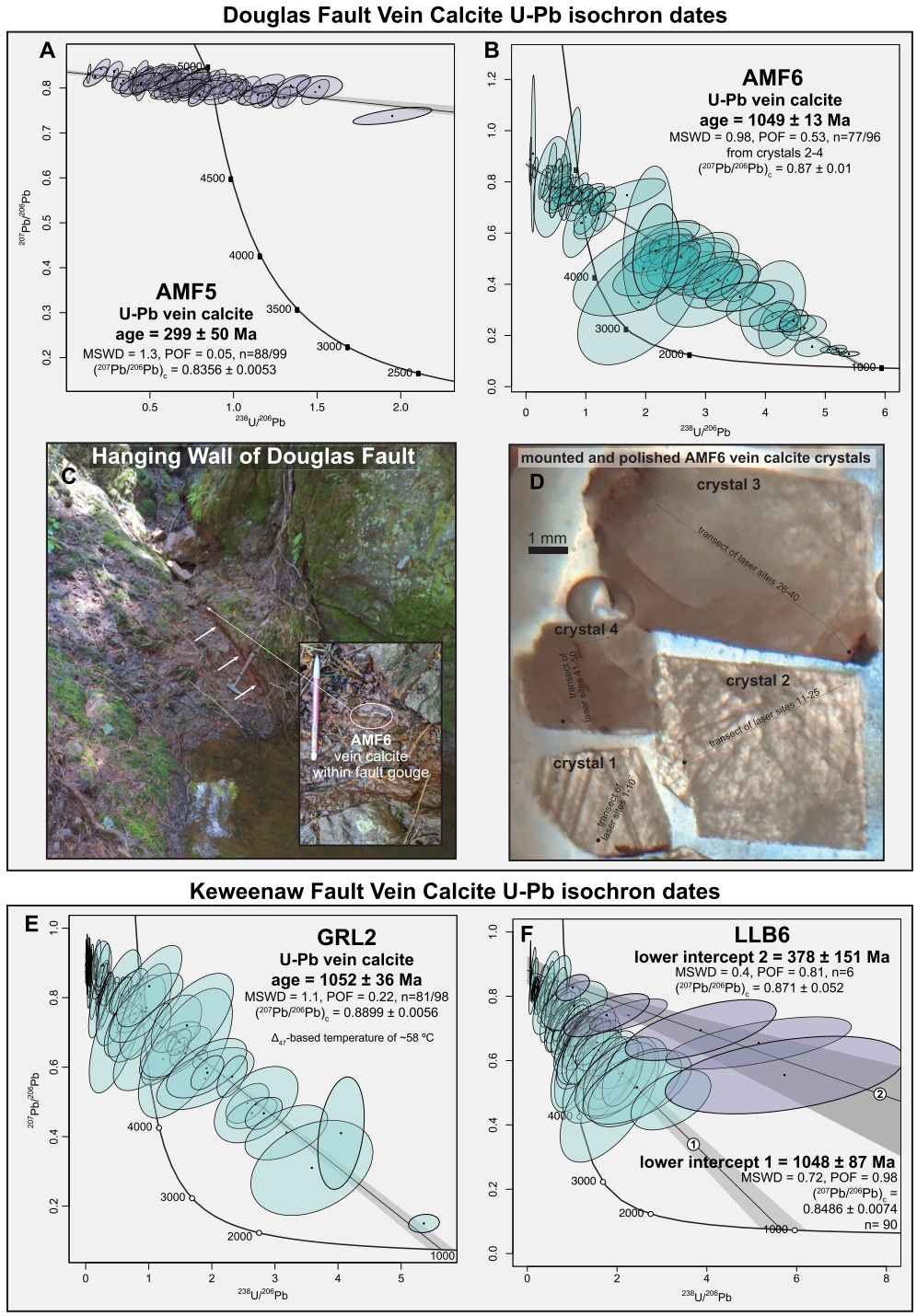

Figure 7. U-Pb data and associated isochron dates of vein calcite samples from the Douglas Fault (Wisconsin) and the Keweenaw Fault (Michigan). (a, b) AMF5 and AMF6 vein calcite samples are from the hanging wall of the Douglas Fault at Amnicon Falls State Park (Figures 3b and 4, Figures S6 and S8 in Supporting Information S1). (c) Field photograph and inset of the hanging wall of the Douglas Fault containing AMF6 vein calcite within red fine-grained fault gouge indicated by white arrows. The fault gouge occurs in the hanging wall ~3 m from the Douglas Fault. (d) Mounted and polished AMF6 vein calcite crystals are shown in transmitted light. The laser transect across each crystal is shown wherein each laser site corresponds to two analyses from two separate laser sessions (Table S4). Crystal 1 of AMF6 did not contain appreciable radiogenic Pb, could not produce an isochron, and had slightly elevated Pb isotopic composition (Figure S3 in Supporting Information S1). Consequently, data from crystal 1 were excluded in the final AMF6 lower intercept date generated from crystals 2–4 (Figure S3 in Supporting Information S1). (e) GRL2 vein calcite is from a brecciated fault zone in the hanging wall of the Keweenaw Fault at Snake Creek Tributary (Table S1 in Supporting Information S1; Figures S5 and S6 in Supporting Information S1). (f) LLB6 vein calcite is from the hanging wall of the Keweenaw Fault near Lac La Belle (Table S1 in Supporting Information S1; Figures S4 and S6 in Supporting Information S1), modified after the U-Pb isochron date in Hodgin, Swanson-Hysell, et al. (2022). The plots were generated and the calculations made using IsoplotR (Ludwig, 1998; Vermeesch, 2018). MSWD, Mean Square Weighted Deviation; POF, Probability of Fit.

including: (a) a time-temperature history of the midcontinent interior implementing the U-Pb calcite—Δ_{47} thermochronometer and relevant compiled data (Figures 8 and 9); and (b) analysis of the erosional history of the midcontinent interior that addresses the tectonostratigraphic setting of the Bayfield-Jacobsville succession and ongoing debate about the magnitude of Cryogenian glacial erosion (Flowers et al., 2020, 2022; Keller et al., 2019; McDannell et al., 2022; Peak et al., 2023).

5.1. Ottawan Inversion of the Douglas Fault

At least 10 km of total vertical displacement has been estimated along the Douglas Fault in northern Wisconsin (Figure 2; Nicholson et al., 2006), which sets the stage for quantifying the amount of displacement during different stages of structural inversion. The onset of structural inversion is constrained using detrital zircon U-Pb geochronology from the uppermost strata of the Oronto Group (upper Freda Formation) (Figure 3; Figure S1 in Supporting Information S1). That the Oronto Group deposition is conformable with the underlying Midcontinent Rift volcanics indicates that it accumulated in the rift basin prior to the contractional inversion that uplifted and tilted the strata (See Section 2.1). Therefore, the timing of initial inversion can be bracketed by a U-Pb detrital zircon maximum age constraint from the upper Oronto Group and by a minimum U-Pb age constraint from post-deformational vein calcite in the hanging wall of the Douglas Fault.

The youngest detrital zircon from the upper Freda Formation dated by CA-ID-TIMS gave a concordant $^{206}Pb/^{238}U$ date of 1051.58 ± 1.11 Ma (Figure 6a), which is interpreted as the maximum depositional age of the uppermost Oronto Group (Section 3 Methods) and the maximum age of structural inversion. Minimum age constraints on the timing of structural inversion come from a sample of post-deformational vein calcite (AMF6) that precipitated within and cross-cuts a fault zone in the hanging wall of the Douglas Fault (Figures 4, 5, and 7). AMF6 yielded a date of 1049 ± 13 Ma (Figure 7b), which is interpreted as the crystallization age of the calcite vein following a period of regional thrust faulting, uplift, and associated deformation. Considering the 2σ uncertainty associated with the maximum and minimum age constraints (1051.58 ± 1.11 Ma is the maximum age constraint, 1049 ± 13 Ma is the minimum age constraint) the detrital zircon and vein calcite U-Pb dates bracket the initial stage of uplift and deformation associated with structural inversion between 1052 Ma and 1036 Ma.

Clumped isotope analyses on the dated vein calcite sample, AMF6, can be used to estimate the temperature at the 1049 ± 13 Ma time of formation and therefore provide insight on emplacement depth. Since low-temperature heating could raise the Δ_{47}-based temperature of the calcite through solid state reordering without resetting its age (Passey and Henkes, 2012; Stolper and Eiler, 2015), the measured Δ_{47}-based temperature can be considered a maximum temperature of formation. AMF6 yields a Δ_{47}-based temperature of 54.4 ± 1.7°C, which is interpreted as the maximum temperature of formation at 1052–1036 Ma following significant structural uplift. It follows that the Chengwatana Volcanics in the hanging wall of the Douglas Fault that underwent greenschist facies metamorphism (Morey, 2001; Wirth et al., 1997) were: (a) buried at least 10 km prior to structural inversion (Nicholson et al., 2006); and (b) uplifted to crustal levels with cooler temperatures within several kms of the paleo-surface prior to vein calcite formation between 1052 and 1036 Ma.

In order to convert the Δ_{47}-based temperature from vein calcite sample AMF6 into an approximate maximum crustal depth at the time of formation, we considered several estimates of regional geotherms for the time interval. One geotherm is derived from a regional metamorphic study of a >2,500-m-thick section of St. Croix Group volcanics in northwestern Wisconsin (Wirth et al., 1997). The calculated geothermal gradient of ~45°C/km is comparable to that determined from metamorphic geothermometry of Midcontinent Rift volcanic strata in northern Michigan (Livnat, 1983). However, more deeply buried strata within the Midcontinent Rift could have been affected by steepening of the geotherm with depth in a continental rift setting (Sandiford and Powell, 1986). Shallower geotherms with a geothermal gradient of 25–30°C/km from the overlying Oronto Group at White Pine in northern Michigan (T. M. Gallagher et al., 2017; Nishioka, 1983) may neglect that the ca. 1050–1030 Ma vein minerals (Bornhorst et al., 1988; Ruiz et al., 1984) could have precipitated during fault-driven uplift rather than during peak burial. Still, other shallow geotherm calculations of ~30°C/km based on clay mineral diagenesis during peak burial (Price and McDowell, 1993) are well-constrained by updated thickness estimates of the Oronto Group (Slotznick et al., 2024; Figure S1 in Supporting Information S1) and may even slightly overestimate burial temperatures. To encompass this uncertainty and range of geotherms for the northern Wisconsin segment of the Midcontinent Rift, we apply a geothermal gradient of 35 ± 10°C/km corresponding to the timing of AMF6 crystallization. A surface temperature of 30 ± 10°C is estimated given the equatorial latitude of Laurentia

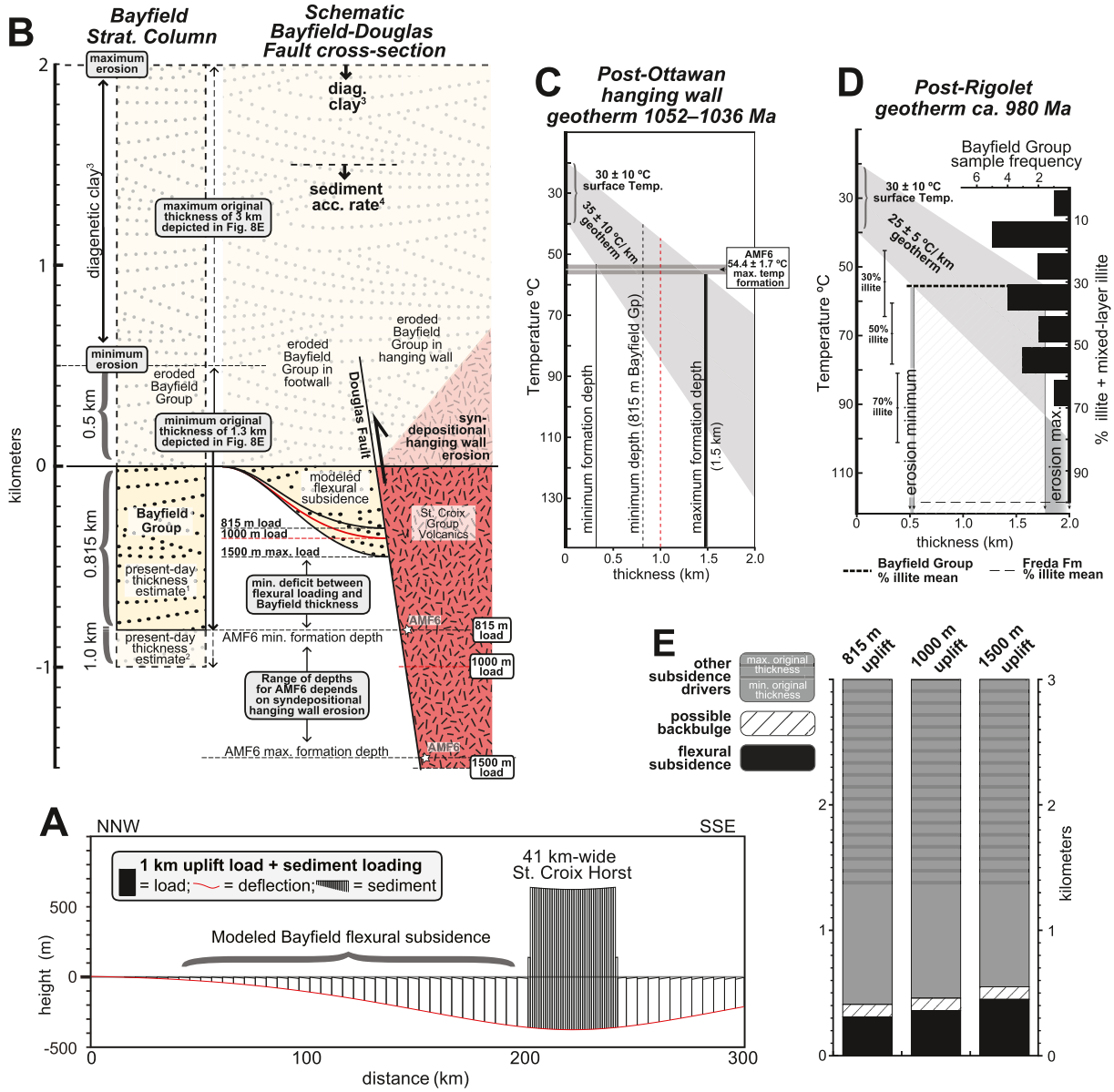

Figure 8. Integrated constraints on Bayfield Group subsidence and St. Croix uplift on the Douglas Fault. (a) Example of flexural modeling run using Flex2D (Cardozo & Jordan, 2001) implementing 1 km of uplift on the St. Croix Horst using the line of section in Figure 2. See Methods and Supporting Information S1 for flexural modeling parameters; (b) Schematic diagram showing thickness of Bayfield Group (left) and Bayfield Group subsidence (right) in response to 815, 1,000, and 1,500 m of St. Croix Horst uplift on the Douglas Fault. Present-day thickness of Bayfield Group[1,2] is estimated as 815 m by Ojakangas et al. (2001) and up to 1,000 m in this study (Section 2.1). The thickness of eroded Bayfield Group strata is constrained by diagenetic clay mineralogy[3] (Figure 8c, Section 5.5, Supporting Information S1), broken foreland basin sediment accumulation rates[4] (Section 5.3; Supporting Information S1), and Δ_{47}-based thermochronometry[5] (Sections 5.1–5.5). White stars represent Δ_{47}-based inferred depth range of vein calcite sample AMF6 following formation ca. 1052–1036 Ma, calculated in Figure 5c; (c) The timing and amount of structural uplift in the hanging wall of the Douglas Fault is calculated from Δ_{47}/U-Pb thermochronometry of vein calcite sample AMF6 using the geotherms discussed in Section 5.1. The thickness of the Bayfield Group in the footwall of the Douglas Fault constrains a minimum amount of uplift following AMF6 crystallization (b); (d) Thermometry data from Dypvik (1983) (left) is calibrated for 30%, 50%, and 70% illite and mixed layer illite. Similar illitization temperatures have been documented in other studies (Salem et al., 2000; Weibel, 1999), and elevated K+ concentrations in the Bayfield Group (Hite, 1968; Myers, 1971) are consistent with illitization occurring at the lower end of its thermodynamic range (Lanson et al., 2002). Percent Illite abundance (right) from outcrop samples of Bayfield Group (Myers, 1971) are plotted in a histogram with 10% bins and displaying mean Bayfield Group and Freda Formation illite abundances. Following re-cratonization of the Midcontinent Rift, we assume a conservative continental geothermal gradient of 25 ± 5°C/km to convert temperature-calibrated % illite abundances to crustal thickness (above present day level of outcrop samples); (e) By applying the minimum and maximum original depositional thicknesses for the Bayfield Group in (b) and 100 m maximum of backbulge subsidence (Currie, 2002; Horton and DeCelles, 1997), relative subsidence contributions are plotted for scenarios involving 815, 1,000, and 1,500 m of St. Croix Horst uplift along the Douglas Fault, highlighting the significant role likely played by other subsidence drivers such as dynamic subsidence (i.e., negative dynamic topography; Heine et al., 2008).

10.1029/2024TC008415

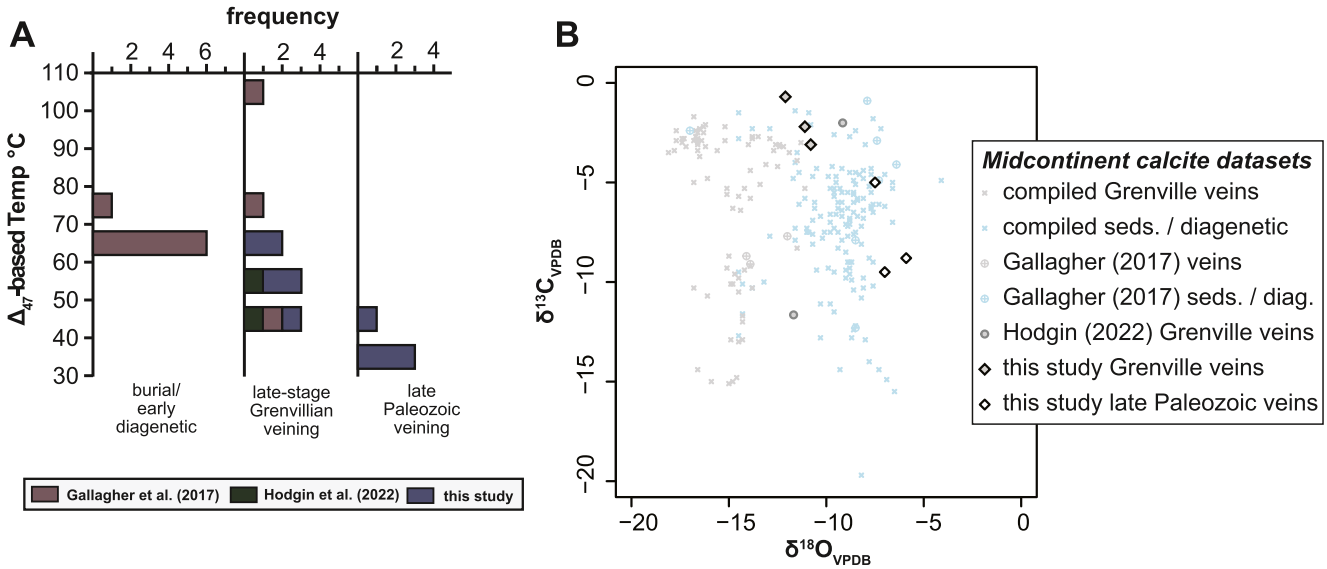

Figure 9. (a) Histogram of compiled Δ_{47}-based temperatures of Midcontinent Rift calcites that formed during pre-Ottawan burial/early diagenesis, Grenvillian mineralization, and late Paleozoic mineralization; (b) Scatterplot of $\delta^{13}C_{VPDB}$ and $\delta^{18}O_{VPDB}$ values of calcites from the Midcontinent Rift. The compiled midcontinent data are from veins or sedimentary/diagenetic calcite samples from Bodden et al. (2022) and Mauk et al. (1992). Data from Bodden et al. (2022) are averages of individual calcite samples analyzed in that study by Secondary Ion Mass Spectrometry, plus compiled data from Bornhorst and Woodruff (1997). Samples from T. M. Gallagher et al. (2017), Hodgin, Swanson-Hysell, et al. (2022), and this study that have Δ_{47}-based temperatures (a) are plotted separately. The sedimentary (seds.) and diagenetic (diag.) calcite samples come from Midcontinent Rift strata that were subjected to burial prior to structural uplift and deformation during Ottawan phase Grenvillian orogenesis.

(latitudinal constraints as in Slotznick et al., 2024) and inferred low paleoelevation (as suggested by Stewart et al., 2023) during Oronto Group deposition. Tropical land temperatures ca. 1050 Ma are uncertain and could have been warmer in a non-glacial climate at the time (such as temperatures as high as 35°C estimated for the Eocene; Zhu et al., 2019). Incorporating appreciably warmer surface temperatures reduces the depth of burial estimates that follow below. According to these parameters, the dated calcite vein in the hanging wall of the Douglas Fault precipitated near the paleosurface. Considering error on the Δ_{47}-based temperature of 54.4 ± 1.7°C, the maximum depth of formation is calculated to be 1.44 km (Figures 8b and 8c). Our estimate of the maximum depth is revised to 1.5 km, which takes into consideration that some undated vein calcite samples from the hanging wall of the Douglas Fault have slightly higher Δ_{47}-based temperatures than the dated AMF6 vein calcite sample (Figure 9; Table S5) and that vertical displacement could be slightly greater along strike. 0.815 km is considered a geological constraint on minimum emplacement depth. This is because the AMF6 calcite vein crystallized prior to Bayfield Group deposition and at least 0.815 km of vertical displacement took place on the Douglas Fault following the onset of Bayfield Group deposition (Figure 8b). The amount of vertical slip that occurred following AMF6 crystallization is therefore constrained to be 0.815–1.5 km (Figures 8b and 8c).

These Δ_{47}/U-Pb data and associated calculations imply that the majority ($\gtrsim$8.5 km) of the $\gtrsim$10 km of total estimated vertical displacement along the Douglas Fault is constrained to have taken place between 1052 and 1036 Ma during the Ottawan phase of the Grenvillian orogeny. The timing and magnitude of the initial inversion of the Douglas Fault is consistent with Ottawan crustal-scale inversion on reverse faults in northern Michigan (Cannon et al., 1993; DeGraff & Carter, 2023), where Ottawan-aged vein calcite is preserved in the hanging wall of the Keweenaw Fault (Figure 7, Figures S4–S6 in Supporting Information S1). The Ottawan-aged vein calcite samples from the Keweenaw Fault have comparable Δ_{47}-based temperatures (Table S5; Figure S5 in Supporting Information S1; Hodgin, Swanson-Hysell, et al., 2022), which can also be interpreted as maximum temperatures of formation that precipitated within 1–2 km of the paleosurface. Therefore, since a similar amount of total vertical displacement has been estimated on the Keweenaw fault (DeGraff & Carter, 2023), this indicates that similar amounts of Ottawan and post-Ottawan vertical displacement occurred on both the Douglas and Keweenaw faults. Taken together, a coherent timing and magnitude of Ottawan structural inversion is inferred across different segments of the Midcontinent Rift. Given that prograde Ottawan metamorphism can be recognized on

the eastern margin of North America as early as ca. 1090 Ma (Swanson-Hysell et al., 2023), this 1052 to 1036 Ma timing of uplift implies a 40–50 Ma lag in the transmission of far-field contractional deformation into the midcontinent. This timing for far-field deposition is closer to the ca. 1050 to 1040 Ma age of peak metamorphic conditions during the long-lived Ottawan phase of the orogeny (Swanson-Hysell et al., 2023).

5.2. Geochronological Constraints on Rigolet Inversion of the Douglas Fault

Post-Ottawan inversion of the Douglas Fault is constrained to less than ∼1.5 km of vertical displacement (Section 5.1; Figure 8), yet the question remains when final inversion took place. In the footwall of the Douglas Fault, the Bayfield Group is deformed by 10 to 100-m-scale drag and fault propagation folds, indicating that there was fault motion following its deposition. Due to uncertainty in the age of the Bayfield Group (Craddock et al., 2013), the timing of its deformation has led to ambiguity on the timing of the Douglas Fault's final significant motion. By using paired LA-ICP-MS and CA-ID-TIMS U-Pb detrital zircon dating (see Section 3) from footwall samples, we accurately and precisely constrained the maximum age of Bayfield Group deposition and its deformation. The youngest CA-ID-TIMS U-Pb detrital zircon $^{206}Pb/^{238}U$ date from the immediate footwall gave a maximum depositional age of 1023.79 ± 0.90 Ma. Sample VNP1, located farther from the fault on the Bayfield Peninsula (Figure 1; Table S1 in Supporting Information S1), had a younger CA-ID-TIMS U-Pb detrital zircon $^{206}Pb/^{238}U$ date of 995.29 ± 1.70 Ma (Figure 6b), which is interpreted as the maximum depositional age of the Bayfield Group. These data demonstrate that motion on the Douglas Fault that folded the Bayfield Group occurred after ca. 1024 Ma, and likely occurred after ca. 995 Ma. The geochronological results are significant in that the Bayfield Group could have been deposited and deformed during the Rigolet phase (1010–980 Ma) of the Grenvillian orogeny, when final inversion of the Keweenaw Fault occurred in northern Michigan (Hodgin, Swanson-Hysell, et al., 2022).

Correlation of the Bayfield Group, in the footwall of the Douglas Fault, with the Jacobsville Formation, in the footwall of the Keweenaw fault (Hamblin, 1958; Van Schmuz and Hinze, 1985), gains new support by both successions containing ca. 995 Ma detrital zircon and thus having similar maximum depositional ages. The correlation is further supported by: (a) new field evidence for syn-depositional and early post-depositional deformation documented in both units (Figure 5; Section 5.3); and (b) paleomagnetic poles from both units that are in a very similar position to one another and distinct from other Mesoproterozoic and Neoproterozoic poles of Laurentia (McCabe and Van der Voo, 1983; Zhang et al., 2024). The correlation implies that the significant exhumation, tilting, erosion, and chemical weathering (up to 10 m deep paleosol profiles) that occurred after Oronto Group deposition and prior to Jacobsville deposition (Gair & Thaden, 1968; B. Gallagher & Bjornerud, 2021; Hamblin, 1958; Kalliokoski, 1975, 1976, 1982; Lewan, 1972), also occurred prior to Bayfield deposition.

5.3. Tectonostratigraphic Setting of the Bayfield Group

Geological constraints on Bayfield Group sedimentation require that its tectono-stratigraphic setting involved syn-depositional and early post-depositional contractional deformation associated with thrust motion on the Douglas Fault. The evidence in support of syn- to early post-depositional deformation in the Bayfield Group comes from: (a) footwall fanglomerates and red clay-rich siltstone beds that pinch out or decrease in abundance away from the Douglas Fault; (b) clastic neptunian dikes penetrating sandstone beds in the footwall and penetrating volcanics in the hanging wall of the Douglas Fault; and (c) a wedge-shaped basin morphology that thickens toward the Douglas Fault, consistent with flexural loading from emplacement of the hanging wall during deposition. Correlation with the Jacobsville Formation brings in additional evidence that gives further insight into the tectono-stratigraphic setting of both the Bayfield and Jacobsville successions.

The clast composition and stratal geometry of Bayfield Group conglomerates in proximity to the Douglas Fault are consistent with syn-depositional faulting. The clast lithologies include an array of basaltic to intermediate volcanic rocks and red fine-grained sandstone, interpreted as derived from the Freda Formation. These lithologies and associated stratigraphic units occur in the hanging wall, or were previously exposed in the hanging wall prior to erosion (Figures 1, 2, and 5). The conglomerate beds of the Bayfield Group exposed in proximity to the Douglas Fault pinch out laterally through the drag folds, such that in equivalent strata >100 m from the fault, the clasts are either rare or absent (Figures 4 and 5). As observed by Myers (1971), the occurrence of red siltstone beds (Figure S7 in Supporting Information S1) also decreases away from the fault, a spatial relationship that can

be explained by weathered volcanic rocks in the hanging wall being the primary source of red silt and clay (Figure S7 in Supporting Information S1). The conglomerate beds deposited adjacent to the active fault are interpreted as wedges of fanglomerate, similar to conglomerates deposited adjacent to active thrust faults in compressional tectonic settings (Song and Wong, 1993) and to analogous deposits in the Jacobsville Formation adjacent to the Keweenaw Fault, which are also associated with red siltstone beds (Brojanigo, 1984; Zhang et al., 2024). The interpretation implies that the Douglas and Keweenaw faults periodically intercepted the paleosurface and shed material from the hanging wall during Bayfield and Jacobsville deposition, respectively (Figure 5).

In addition to syn-depositional faulting, continued movement of the fault immediately following deposition is required by the presence of clastic neptunian dikes that penetrate basalt in the hanging wall. The sandstone dikes are composed of sand that match the color, texture, and composition of deformed Bayfield Group sandstone in the footwall (Figure 4). Sandstone dikes have also been documented within the Orienta Formation near the Douglas Fault at Amnicon River (Hite, 1968). The occurrence of the clastic dikes suggests that the Orienta Formation was unlithified and still contained water such that it became overpressured at the time the hanging wall was emplaced above it during contractional deformation. This overpressuring would have led to clastic dike emplacement as observed in other compressional basins undergoing active thrusting (Winslow, 1983). Similar clastic dikes of Jacobsville sandstone cross-cut the Jacobsville Formation (Hamblin, 1958) and cross-cut basalt in the hanging wall of the Keweenaw Fault on the Keweenaw Peninsula, where the sandstone dikes were also interpreted as syn-tectonic (Cornwall, 1955). Growth strata are well-documented in basal Jacobsville deposits (Hedgman, 1992), which further suggests that both the onset of deposition and deformation of the Jacobsville occurred within a compressional tectonic setting. Fold tests on pigmentary hematite magnetization in the Jacobsville Formation in the footwall of the Keweenaw fault also support the interpretation that deformation of the Jacobsville occurred soon after deposition (Zhang et al., 2024).

The Bayfield and Jacobsville successions occur as wedge-shaped basins that thicken toward the Douglas and Keweenaw faults, respectively. The wedge-shaped basin morphology is consistent with flexural loading from emplacement of the hanging wall coinciding with footwall deposition. Such an interpretation is consistent with the geological evidence presented above for syn-depositional thrust fault motion and associated deformation in the Bayfield Group and Jacobsville Formation. Wedge-shaped compressional basins that thicken toward a fault and accumulate sediment during hanging wall uplift are generally classified as foreland basins. Given the great distance (>500 km) from the Grenville Front (Figure 1), the Bayfield basin could be interpreted as an isolated, or broken, foreland basin (Horton et al., 2022; Strecker et al., 2011). Paleocurrents from the Bayfield-Jacobsville successions indicate some transverse and predominantly axial transport (Hedgman, 1992; Kalliokoski, 1982; Myers, 1971) as observed in and along the main channels of fluvial systems in foreland basins (Burbank & Raynolds, 1988; Fedo et al., 2003). That the Rigolet phase of the Grenvillian Orogeny is constrained in age between 1010 and 980 Ma (Swanson-Hysell et al., 2023) and that the age of the Bayfield Group can be constrained to <995 Ma implies a relatively narrow age range for the deposition and deformation of the Bayfield Group, if it were deformed by late Grenvillian far-field orogenesis. The evidence for syn-depositional and early post-depositional fault movement supports this interpretation, and it suggests that both deposition and deformation of the Bayfield Group are linked to late Grenvillian far-field orogenesis within a broken foreland basin.

5.4. Flexural Modeling and Basin Analysis of the Bayfield Group

It was recently proposed that the Jacobsville Formation and Bayfield Group could have been deposited in a Grenvillian back-bulge setting during the Rigolet phase of the Grenvillian orogeny (Hodgin, Swanson-Hysell, et al., 2022) associated with the ca. 980 Ma development of the Grenville Front (Krogh, 1994; Rivers et al., 2012). The location of the Midcontinent Rift with respect to the Grenville Front (Figure 1) could be consistent with a back-bulge setting. However, flexural subsidence associated with the backbulge itself is not sufficient to explain the thickness of the strata. Rather, ≥1 km of subsidence in each of the Jacobsville and Bayfield basins is at least an order of magnitude greater than the typical thickness of backbulge deposits (Currie, 2002; Horton and DeCelles, 1997; Figure 8e). Another potential subsidence mechanism is flexural loading from the hanging wall during fault emplacement, which is consistent with the wedge-shaped basins and deeper depocenters of the Bayfield and Jacobsville successions adjacent to the Douglas and Keweenaw thrust faults, respectively (Section 5.3; Figures 2 and 8).

To investigate the role played by flexural subsidence, our 2D flexural modeling of the Bayfield basin estimates flexural subsidence in response to uplift of the 41-km wide St. Croix Horst in the hanging wall of the Douglas Fault (Figure 8; Supporting Information S1). The modeled scenarios involving loads of 815, 1,000, and 1,500 m are tuned by geological constraints. The present-day geometry of the Douglas Fault and the Bayfield Group requires at least 815 to 1,000 m of St. Croix Horst uplift during Bayfield deposition (Figure 8b; Nicholson et al., 2006; Ojakangas et al., 2001), which would have driven 310–360 m of flexural subsidence with the chosen model parameters (Section 3; Figure 8b; Supporting Information S1). Assuming a maximum post-Ottawan uplift of 1.5 km (Section 5.1) and that all displacement occurred during Bayfield deposition, it would result in flexural subsidence of ∼450 m, including the loading from sediment deposited in the accommodation space (Figures 8b and 8e; Figure S9 in Supporting Information S1).

Given that the original thickness of the Bayfield Group was at least 815 to 1,000 m (Section 5.5; Figure 8b; Ojakangas et al., 2001) and that flexural subsidence can only account for 310–450 m, other drivers of subsidence are required. Taking into consideration that the original thickness of the Bayfield Group would have been thicker prior to erosion, this requires even greater contributions from other subsidence drivers (Figure 8e). To better quantify the amount of additional subsidence, the original thickness of the Bayfield Group was estimated from its low-grade metamorphic clay assemblage and from its estimated sediment accumulation rate (Figure 8b; Supporting Information S1). By applying empirical clay mineral transformation temperatures to the metamorphic clay assemblage of the Bayfield Group (Myers, 1971) a burial depth range can be estimated (Figures 8b and 8d). Since distinct clay transformation pathways that lead to the same metamorphic clay assemblage can take place at different burial temperatures (Lanson et al., 2002), it is essential to develop some constraints on the clay assemblage at the time of deposition. The common occurrence of mixed layer illite/chlorite in the Bayfield Group (Myers, 1971), including expandable mixed layer illite/chlorite, indicates that smectite was a significant precursor clay mineral (Eberl et al., 1986; Lanson et al., 2002; Środoń, 1999) prior to burial diagenesis. Given that smectite is a common product in the earliest weathering phases of basaltic rocks (Smith et al., 1987), its occurrence could be expected in the rift basin, although we note that mafic rocks and minerals are readily transformed to kaolinite in tropical climates (Fisher & Ryan, 2006; Pett-Ridge et al., 2007; Sak et al., 2004). Authigenic smectite is also common in floodplain deposits that undergo wetting and drying cycles in monsoonal climates (Huyghe et al., 2011), which is consistent with the inferred climatic, depositional, and tectonic setting of the Bayfield Group. The occurrence of disordered kaolinite as the primary kaolinite type in the Bayfield Group (Myers, 1971), likely indicates formation from a smectite precursor during post-depositional near-surface weathering (Amouric & Olives, 1998; Fisher & Ryan, 2006). Therefore, we infer that the precursor clay minerals of the Bayfield Group prior to burial diagenesis consisted of a mixture of both smectite and kaolinite.

Temperatures of the illitization of smectite have been characterized in petroleum basins, where the loss of abundant smectite in favor of illite formation begins to occur at 35–60°C (Dypvik, 1983; Środoń and Eberl, 1984; Weibel, 1999) followed by chlorite formation at 70–75°C (Weibel, 1999; Worden and Morad, 2009), although lower temperatures of diagenetic chlorite formation have been documented (Beaufort et al., 2015; Chang et al., 1986). The clay composition of the Bayfield Group near the surface (∼32% illite and mixed-layer illite; Figure 8d) is similar to fluvial successions that were buried to temperatures of 35 to 65°C (Figure 8d; Dypvik, 1983; Salem et al., 2000). Chlorite, which occurs at either trace levels or is absent in upper strata, commonly occurs in low abundance in the most deeply buried strata of the Bayfield Group (Myers, 1971), which is consistent with its formation by burial diagenesis. Below the Bayfield Group, the underlying Freda Formation, which was subjected to ∼100–125°C burial temperatures (T. M. Gallagher et al., 2017; Mauk and Hieshima, 1992; Price and McDowell, 1993) can have an illite value approaching 100% (Myers, 1971). Given the lower metamorphic grade of the Bayfield Group compared to the underlying Freda Formation, this suggests that lower temperatures in the Bayfield Group associated with burial diagenesis are reasonable. Assuming illite formation primarily from kaolinite and at >90°C (Lanson et al., 2002) is therefore inconsistent with the differences in metamorphic grade between the Freda Formation and Bayfield Group. We note that illite formation from kaolinite can occur at temperatures of ≳70°C (Akinlotan et al., 2022; Worden and Morad, 2009) or at even lower temperatures in the presence of brines (Freiburg et al., 2022; Grathoff et al., 2001). Elevated potassium cation concentrations in the Bayfield Group (Hite, 1968; Myers, 1971) are consistent with illitization occurring at the lower end of its thermodynamic range (Lanson et al., 2002) and elevated boron concentrations within fluvial facies of the Bayfield Group (Myers, 1971) are also consistent with the influence of diagenetic brines.

By assuming a surface temperature of 30 ± 10°C and a geothermal gradient of 25 ± 5°C/km, the clay assemblage data from Myers (1971) are used to estimate a burial depth range (Figure 8d). Using a linear extrapolation, illite and mixed-layer illite thermometry data from Dypvik (1983) were applied to corresponding illite and mixed-layer illite percentages from the Bayfield Group (Figure 8d). From this calculation, the preserved Bayfield Group is estimated to have been buried by 533 to 1,817 m of additional strata. Given underlying uncertainties in the clay transformation temperature calibrations, we more conservatively revise the estimated range of additional burial to 0.5–2 km. The 0.5–2 km estimate of eroded Bayfield strata therefore yields an original Bayfield Group thickness of 815–1,000 m (preserved) + 500–2,000 m (eroded), or 1,315–3,000 m (Figures 8b and 8e). The minimum original thickness (1,315 m) in the stacked bar chart of Figure 8e is shown as a function of the different contributors to total subsidence. As a point of comparison to the 0.5–2 km estimate of eroded Bayfield strata, our sediment accumulation rate analysis (Figure 8b; Supporting Information S1) implies a maximum of 1,500 m of additional strata. These estimates underscore that: (a) significant erosional removal of Bayfield Group strata occurred, although less than 1.5–2 km; and (b) flexural loading can account for only ¼ to ⅕ of total Bayfield subsidence (Figure 8e), which must therefore be explained by other subsidence drivers.

One potential mechanism that could explain additional subsidence is lingering thermal subsidence as upwelled asthenosphere during rifting and a localized magmatic underplate (Chichester et al., 2018) continued to cool even after 10–30 km of Ottawan crustal inversion in the Midcontinent Rift (Cannon et al., 1993). In continental rift basins undergoing inversion, there can be competing effects of lingering subsidence through postrift cooling and sediment loading versus uplift resulting from contraction (Oravecz et al., 2024). These competing effects can lead to temporal and spatial variations in subsidence versus uplift modulated by the rate of contractional deformation (Oravecz et al., 2024). During Bayfield deposition, contractional deformation and local uplift resulted in the hanging wall penetrating the surface while residual thermal subsidence could have been a driver of broader regional subsidence. One challenge of invoking significant contributions from lingering thermal subsidence is the significant time gap between Ottawan deformation and subsequent Bayfield-Jacobsville sedimentation and that the onset and duration of Bayfield-Jacobsville deposition is temporally, structurally, and sedimentologically linked with contractional deformation.

Another potential mechanism is dynamic subsidence (i.e., negative dynamic topography) associated with mantle downwelling (Heine et al., 2008). The closure of the Unimos Ocean with Laurentia on the lower plate drove rapid plate motion leading up to Grenvillian collisional orogenesis (Swanson-Hysell et al., 2019, 2023). Long-lived contraction during the Grenvillian orogeny could be associated with the orogen remaining atop a zone of downwelling that was established during the subduction that closed the ocean basin (Swanson-Hysell et al., 2019). Paleomagnetic data from the Jacobsville Formation (Zhang et al., 2024) establish that Laurentia slowly drifted over the position in the asthenosphere where subduction had previously occurred by the time of Jacobsville-Bayfield Group deposition (Figure S10 in Supporting Information S1). In this position, there is the possibility that continued downwelling mantle flow induced broad lithospheric subsidence.

Another mechanism to consider is long-wavelength dynamic subsidence linked to subduction-related mantle flow beneath Laurentia, as observed in the Cretaceous foreland of the Cordilleran Laramide orogeny involving subduction under Laurentia's western margin (Li and Aschoff, 2022; Mitrovica et al., 1989). Such a mechanism has the appeal of being consistent with the timing of Rigolet phase orogenesis. However, considering that Laurentia was on the lower plate of the Grenvillian collision (Hynes and Rivers, 2010), it may be infeasible to invoke this mechanism. Yet, there is significant uncertainty in Grenvillian reconstructions due largely to subsequent tectonic fragmentation (Cordani et al., 2005; Ramos, 2010) of the once wider Grenville orogen (Hynes and Rivers, 2010; Rivers et al., 2012). The possibility of subduction, and associated dynamic subsidence, beneath Laurentia during the Rigolet could thus remain possible since commonly identified conjugate terranes with Grenvillian basement, such as Oaxaquia, have been interpreted as having a potential west-dipping subduction zone beneath outermost/easternmost structural domains (Cawood & Pisarevsky, 2017; Keppie and Gutiérrez, 2010; Solari et al., 2003). While such unresolved aspects of the Grenville orogen are beyond the scope of this paper, we may not be able to rule out a scenario involving long-wavelength dynamic subsidence under a once much wider Grenville orogen that was initiated during the Rigolet phase.

Finally, we address the expected spatial distribution of sedimentation associated with the potential mechanisms for driving the required additional Bayfield-Jacobsville subsidence and whether correlative units outside the Midcontinent Rift are preserved on Laurentia. Some of the potential driving mechanisms, such as backbulge

flexure or lingering thermal subsidence, would have been more spatially restricted to the Midcontinent Rift, whereas other dynamic mechanisms could have resulted in broader continental-scale subsidence consistent with the hypothesized "Great Grenvillian sedimentation episode" (Rainbird et al., 2011). A continental-scale subsidence mechanism could explain distal remnants of a widespread transcontinental Grenvillian fluvial system preserved within the Amundsen and Mackenzie basins in northwestern Canada that are potentially the same age as the Bayfield-Jacobsville successions (Greenman et al., 2021; Rainbird et al., 2017; Rayner and Rainbird, 2013; van Acken et al., 2013). Existing geochronological, lithological, provenance, and paleocurrent data (Ielpi and Rainbird, 2016; Rainbird et al., 1992, 2011, 2017) support the existence of a late-Grenvillian transcontinental fluvial system to which the Bayfield-Jacobsville may have been connected (Fedo et al., 2003; Rainbird et al., 2011). Other provenance studies also support the existence of transcontinental rivers originating from the Grenville orogen extending into southwestern Laurentia (Fedo et al., 2003; Hantsche et al., 2021; Howard et al., 2015). If disparate remnants of ca. 1000 Ma fluvial successions can be correlated, then a continental-scale dynamic mechanism may be required to explain the Bayfield-Jacobsville foreland system within a vast, transcontinental framework.

5.5. Late Paleozoic Calcite Precipitation and Constraints on Regional Exhumation

Late-stage vein calcite from the Douglas Fault can be used to assess post-Grenvillian fault reactivation and to gain additional insight on the time-temperature history of the region between ca. 980 Ma and the present. Sample AMF5, which comes from a thin calcite vein along the Douglas Fault plane, yielded a U-Pb lower intercept date of 298.5 ± 50.3 Ma (Figure 7a) and a Δ_{47}-based temperature of 33.0°C. An overlapping Paleozoic U-Pb calcite isochron date of 378 ± 151 Ma from Keweenaw Fault zone sample LLB6 (Figure 7f and Figure S4 in Supporting Information S1; Hodgin, Swanson-Hysell, et al., 2022), suggests that Paleozoic fault reactivation in the Midcontinent Rift is regional in extent. Where Paleozoic reactivation of thrusting on the Douglas Fault has been documented, the maximum associated offset is ~60 m (Setterholm, 2010). The $\delta^{13}C$ and $\delta^{18}O$ values of the ca. 300 Ma calcite are similar to those from AMF2 and AMF3 (Figure 9b), which are from thin, fibrous calcite veins that formed by a crack-seal mechanism in a tensional stress regime directly on or immediately adjacent to the Douglas Fault plane. The latter samples, which are considered the latest stage of calcite generation because they are undeformed and effectively seal the fault, have a similar Δ_{47}-based temperature of 38.3 ± 2.3°C (Figure 9a). These results are interpreted to indicate that minor far-field contractional stress associated with minimal thrust fault reactivation and fluid mobilization was transmitted into the midcontinent in the Paleozoic, potentially during the continent-continent collision of the Alleghanian orogeny (Hatcher et al., 1989). The data are interpreted to constrain nearly all post-Ottawan slip on the Douglas Fault as occurring during the Rigolet phase of the Grenvillian orogeny. The ~35°C temperature of ca. 300 Ma late-stage calcite and associated fibrous vein calcite is consistent with minor burial under several hundred meters of Paleozoic strata prior to Pleistocene glacial erosion. The study sites escaped more significant km-scale Paleozoic deposition and Mesozoic unroofing that occurred to the northeast, in southern Ontario (Sturrock et al., 2024), as well as more significant Paleozoic deposition to the south, in the Illinois Basin (Freiburg et al., 2022). While there are sites nearby, such as the Lake Superior basin, where more significant Pleistocene subglacial erosion occurred (Wright, 1973), the region of our study sites in northern Wisconsin and Michigan underwent comparatively less Pleistocene glacial erosion (Naylor et al., 2021). During the Phanerozoic, the study sites in northern Wisconsin in proximity to the Wisconsin Arch (Bunker et al., 1988) have therefore been comparatively stable in the midcontinent region.

5.6. Constraints on the Great Unconformity

The cratonic interior of North America has been identified as an important testing grounds for the debated timing, mechanisms, and total amount of continental erosion over the last billion years (McDannell et al., 2022; Peak et al., 2023). In particular, potentially low long-term erosion rates in the cratonic interior make the region ideal for constraining continental erosion minima, which can be used to differentiate between models that make differing predictions of the amount and timing of erosion prior to the transgression that formed the Great Unconformity. Our study sites are located in proximity to regional exposures of the Great Unconformity, which consists of a sharp depositional contact between Cambrian marine sandstones and the underlying Precambrian rocks (Figure 1; Hamblin, 1958; Runkel et al., 2007; Sloss, 1963), representing a hiatus of ≥475 Ma (Hodgin, Swanson-Hysell, et al., 2022). The Great Unconformity can be subtle in the region, juxtaposing low-grade, flat-lying Cambrian sandstone above low-grade, flat-lying early Neoproterozoic sandstone (Hamblin, 1958; Hodgin, Swanson-Hysell,

et al., 2022). A glacial origin of the Great Unconformity has been proposed to be associated with widespread 3–5 km of upper crustal continental erosion during the Cryogenian Period (Keller et al., 2019; McDannell et al., 2022), whereas a tectonic origin has predicted multiple episodes of erosion (Flowers et al., 2020; Peak et al., 2023). The low-grade and generally flat-lying Bayfield Group and equivalents that underlie Cambrian strata represent a potential erosion minimum of this iconic hiatus.

New constraints compiled and analyzed in the previous section suggest that no more than 0.5–2 km of erosion took place between the end of Bayfield Group deposition ca. 980 Ma and the onset of Cambrian deposition. This amount of upper crustal erosion is less than the 3–5 km argued by the hypothesis that Cryogenian subglacial erosion created the Great Unconformity (Keller et al., 2019; McDannell et al., 2022) although those workers have noted that glacial erosion is expected to be spatially heterogeneous. The data compiled here indicate that this region could not have been one that was deeply eroded during the Cryogenian. As presented in Hoffman (2023), rates that have been calculated for Snowball Earth glacial sediment accumulation are an order of magnitude less than those implied by the Keller et al. (2019) erosion magnitude. The hypothesis of minimal subglacial erosion for much of the duration of the Cryogenian Snowball Earth glaciation can be supported by observations of minimal subglacial erosion for 10s of Myr, and even protective shielding of ancient topography, beneath the East Antarctic Ice Sheet (Cox et al., 2010; Creyts et al., 2014; Jamieson et al., 2010).

The setting of the East Antarctic Ice Sheet may be the best Snowball ice sheet analog on Earth (Hoffman et al., 2017) given interpretations of a weak hydrologic cycle during the Snowball climate state (Abbot, 2014; Abbot et al., 2013; Goddéris et al., 2011; Hoffman et al., 2017; Pierrehumbert et al., 2011; Voigt, 2013). Glacial erosion associated with Cryogenian glaciation would therefore be concentrated during the interval of Snowball meltback when there could have been dynamic wet-based and erosive ice sheets. Further analyses from the region will be required to more precisely determine the amount (∼0.5–2 km) of post-Grenvillian erosion and how much can be attributed to Cryogenian subglacial erosion versus Cryogenian-Ediacaran regional exhumation (Figure 10; Peak et al., 2023).

6. Summary and Conclusion

In this study, we present an updated history of Midcontinent Rift structural inversion that assesses the timing and magnitude of far–field orogenesis. Thermal subsidence in the Midcontinent Rift was ongoing until at least 1052 Ma, as constrained by a new CA-ID-TIMS U-Pb maximum depositional age constraint on detrital zircon from the upper Freda Formation of the Oronto Group in northern Michigan. Subsequent structural inversion of the Midcontinent Rift along the Douglas Fault in northern Wisconsin is constrained by post-deformational vein calcite dated by U-Pb LA-ICP-MS geochronology in its hanging wall at 1049 ± 13 Ma. Combined, the U-Pb zircon and U-Pb vein calcite dates bracket the initial stage of structural inversion to have occurred between 1052 and 1036 Ma, during the Ottawan phase of the Grenvillian orogeny. Using clumped isotope analyses, the dated Ottawan vein calcite also yielded a maximum temperature of formation, pertaining to an interpreted crustal depth of ∼1–1.5 km. This indicates that of the ∼10 km of total estimated vertical displacement on the Douglas Fault that 8.5–9 km had occurred by the time the vein calcite formed between 1052 and 1036 Ma. That the majority of structural inversion along the Douglas Fault occurred during Ottawan far–field orogenesis is consistent with thermochronometric data from the Keweenaw Fault in northern Michigan (Figure 7, Figures S4 and S5 in Supporting Information S1) and from other thrust faults that accommodated structural inversion of the Midcontinent Rift (Cannon et al., 1993). The timing of Ottawan structural inversion in the Midcontinent Rift began 40–50 Ma after the onset of Ottawan orogenesis in eastern North America, indicating a significant delay in the transmission of far-field orogenesis into the continent interior.

Following Ottawan structural inversion, which deformed and tilted the underlying Midcontinent Rift strata, an interval ensued that involved significant landscape incision and paleosol development (Hamblin, 1958; Kalliokoski, 1975; Lewan, 1972). The Bayfield Group, which is deformed by drag and fault propagation folds in the footwall of the Douglas Fault, was deposited on the underlying Midcontinent Rift strata with angular unconformity, and was therefore deformed by post-Ottawan motion on the fault. The youngest detrital zircon from the Bayfield Group dated by CA-ID-TIMS yields a maximum depositional age of 995.29 ± 1.70 Ma, which supports its correlation with the <993 Ma Jacobsville Formation in northern Michigan (Hodgin, Swanson-Hysell, et al., 2022). Our interpretation of the onset of Bayfield Group deposition is informed by geological evidence of a hiatus following Ottawan inversion (Hamblin, 1958), new maximum depositional age constraints (Figure 6), and by widespread evidence of syn-sedimentary thrust faulting in a compressional stress regime. Bayfield Group

10.1029/2024TC008415

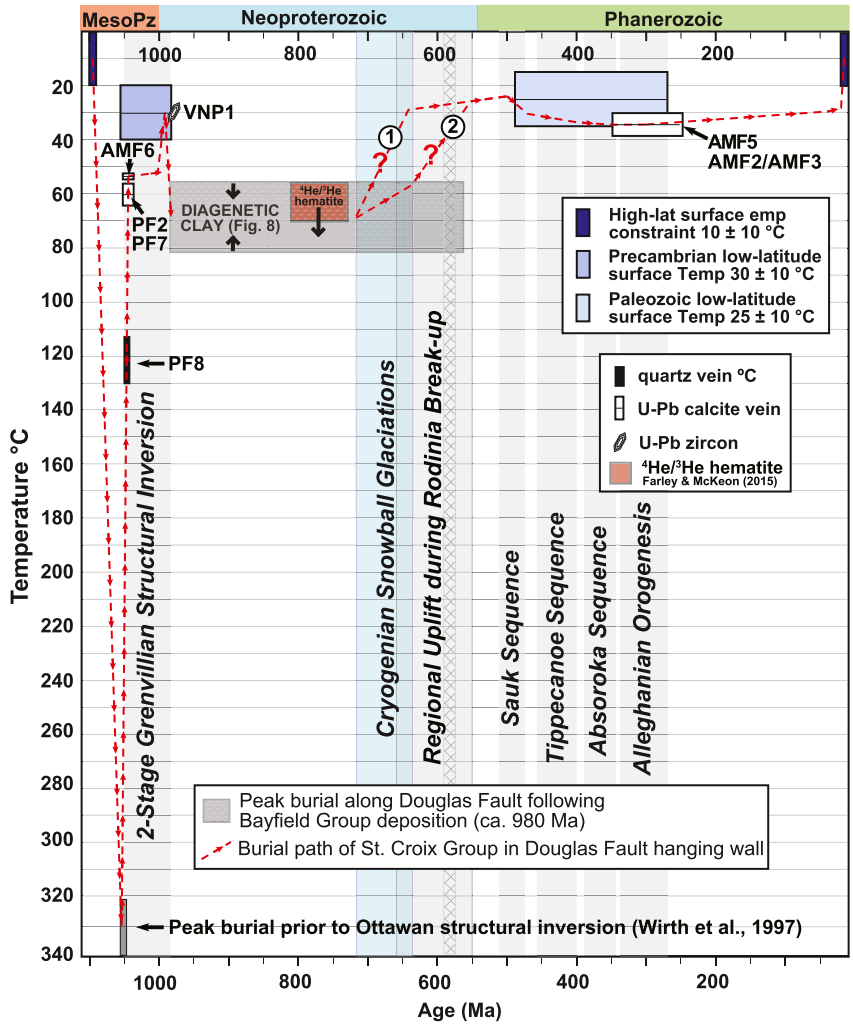

Figure 10. Time-temperature path for paired Δ_{47}/U-Pb calcite thermochronometry compiled with existing data on peak metamorphism in the Chengwatana basalt (Wirth et al., 1997) and Bayfield Group (Myers, 1971). Low-latitude surface temperatures (Slotznick et al., 2024; Swanson-Hysell and Macdonald, 2017; Zhang et al., 2024) are assigned as 30 ± 10°C for the Precambrian and 25 ± 10°C for the Paleozoic (Section 5.1); mid- to high-latitude surface temperatures (Swanson-Hysell et al., 2019) are assigned as 10 ± 10°C. The cross-hatched interval in Regional Uplift during Rodinia Breakup is from 590 to 577 Ma, the interval of extensive regional uplift in the midcontinent based on regional U-Th/He data (Peak et al., 2023). Slightly older (<650 Ma) regional tectonic uplift is permitted from the U-Th/He data of Sturrock et al. (2021). Neoproterozoic uplift and erosion scenario 1 is driven primarily by Cryogenian subglacial erosion in the scenario of Keller et al. (2019), though with smaller magnitude of erosion. The minimum $^4He/^3He$ hematite temperature constraint shown (sample: MI-81; Farley & McKeon, 2015) is from the study region just east of the Wisconsin-Michigan border. Thermal uncertainty from MI-81 is due to the sample coming from an unknown depth 0–750 m below the base of the Jacobsville Formation, which is correlated with the Bayfield Group. Neoproterozoic uplift and erosion scenario 2 is driven primarily by uplift during break-up of the supercontinent Rodinia (Peak et al., 2023).

fanglomerates in the footwall of the Douglas Fault, clastic dikes of Bayfield Group sandstone in the hanging wall of the Douglas Fault (Figures 4 and 5), and a wedge-shaped basin morphology adjacent to the Douglas Fault provide evidence of syn- to early post-depositional fault motion in a flexural foreland basin. Footwall fanglomerates of the Jacobsville Formation (Brojanigo, 1984; Hodgin, Swanson-Hysell, et al., 2022; Zhang et al., 2024), associated clastic dikes in the hanging wall of the Keweenaw Fault (Cornwall, 1955), and a wedge-shaped basin morphology adjacent to the Keweenaw Fault are also observed in northern Michigan, indicating that the correlated Bayfield and Jacobsville units both experienced syn- to early post-depositional deformation in correlative foreland basin systems during the 1010–980 Ma Rigolet phase of the Grenvillian Orogeny.

On top of the 0.8–1 km of Bayfield Group strata that are currently preserved in the footwall of the Douglas Fault, our basin analysis demonstrates the accumulation of an additional 0.5–2 km of now-eroded Bayfield Group strata. This analysis permits an assessment of Bayfield-Jacobsville basin-forming mechanisms that informs the subsequent tectonic and erosional history of the region. Flexure due to thrust fault uplift is identified as an important contributor to the overall subsidence of Bayfield-Jacobsville basin formation and minor contributions from back bulge subsidence and lingering thermal subsidence are possible, yet the dominant contributor to Bayfield-Jacobsville subsidence was likely due to dynamic subsidence. Given that Laurentia was on the lower plate of the Grenvillian collision, long wavelength mantle flow associated with subduction under Laurentia likely cannot be invoked. Instead, we propose another scenario in which the closure of the Unimos Ocean with Laurentia on the lower plate, which drove rapid plate motions leading up to Grenvillian collisional orogenesis (Swanson-Hysell et al., 2019, 2023), was associated with a vigorous downwelling zone in the mantle. Paleomagnetic data from the Jacobsville Formation (Zhang et al., 2024) establish that during the Grenvillian orogeny Laurentia slowly drifted over the position in the asthenosphere where subduction had previously occurred by the time of Jacobsville/Bayfield Group deposition (Figure S10 in Supporting Information S1). In this position, there is the possibility that mantle flow induced lithospheric subsidence (Heine et al., 2008). A continental-scale driver of dynamic subsidence may be required if basins interpreted as transcontinental fluvial systems in northwestern Laurentia that carry late-Grenvillian detritus are correlative with the Bayfield-Jacobsville (Ielpi and Rainbird, 2016; Rainbird et al., 1992, 2011, 2017; Rayner and Rainbird, 2013).

In combination with other data sets and basin analysis, the method of Δ_{47}/U-Pb calcite thermochronometry (Looser et al., 2021; Mangenot et al., 2018) is used to infer a time-temperature and erosional history of the region. The data imply less than 2 km of additional Bayfield Group strata and less than 2 km of erosion below Cambrian strata. The Bayfield Group and Jacobsville Formation may thus be vestiges of an extensive late-Grenvillian foreland basin, that was largely eroded by subglacial Cryogenian glaciation (Keller et al., 2019) and/or by tectonic uplift during break-up of the supercontinent Rodinia (Peak et al., 2023). The results from the Midcontinent Rift highlight the existence of a North American Neoproterozoic erosion minimum of less than 2 km below Cambrian strata that mark the Great Unconformity. This amount of erosion contrasts with the 3–5 km predicted by a Neoproterozoic glacial origin of the Great Unconformity (Keller et al., 2019).

Late-stage (ca. 300 Ma) vein calcite along the Douglas and Keweenaw faults was also identified, which likely formed due to the transmission of far-field stress into the midcontinent during Paleozoic orogenesis. We note that Paleozoic orogenesis has been linked to no more than ~60 m of displacement along the Douglas Fault (Setterholm, 2010). This restricts the timing of major km-scale episodes of far-field orogenesis into the North American midcontinent interior as occurring during Grenvillian orogenesis. Δ_{47}-based thermochronometry from Paleozoic vein calcite samples is approximately consistent with surface temperatures at the time (Peppers, 1996; Roark et al., 2017), suggesting that minimal uplift or erosion has occurred in the study area since the Paleozoic. The Paleozoic constraints on far-field orogenesis aid in clarifying that the final stage of significant inversion occurred during the Rigolet phase of the Grenvillian orogeny and that our study area in the cratonic interior of North America has remained remarkably stable for nearly a billion years.

Data Availability Statement

The data and software needed to understand and evaluate the reported research can be found in the main text, supplement, and references. All data associated with the manuscript will also be made available within a Github repository specifically associated with this work at https://github.com/Swanson-Hysell-Group and archived on Zenodo (https://zenodo.org).

Acknowledgments
This research was supported by U.S. National Science Foundation CAREER Grant EAR-1847277 to N.L. Swanson-Hysell and a UC Berkeley Esper S. Larsen Jr. Fund Grant to N.L. Swanson-Hysell and E.B. Hodgin. We thank J. Crowley and D. Schwartz at Boise State University (Boise, Idaho, USA), and J. Grimsich at the University of California, Berkeley, for assistance. The Wisconsin Department of Natural Resources is acknowledged for granting a research and collection permit that enabled sampling. Associate Editor Dr. Alexis Ault and two anonymous reviewers are thanked for their constructive reviews.

References

Abbot, D. S. (2014). Resolved Snowball Earth clouds. *Journal of Climate*, *27*(12), 4391–4402. https://doi.org/10.1175/JCLI-D-13-00738.1

Abbot, D. S., Voigt, A., Li, D. W., Le Hir, G., Pierrehumbert, R. T., Branson, M., et al. (2013). Robust elements of Snowball Earth atmospheric circulation and oases for life. *Journal of Geophysical Research: Atmospheres*, *118*(12), 6017–6027. https://doi.org/10.1002/jgrd.50540

Abruzzese, M. J., Waldbauer, J. R., & Chamberlain, C. P. (2005). Oxygen and hydrogen isotope ratios in freshwater chert as indicators of ancient climate and hydrologic regime. *Geochimica et Cosmochimica Acta*, *69*(6), 1377–1390. https://doi.org/10.1016/j.gca.2004.08.036

Adamson, K. F. (1997). Petrology, stratigraphy and sedimentation of the Middle Proterozoic Bayfield Group, northwestern Wisconsin [M.S. thesis] (p. 238). University of Minnesota.

Akinlotan, O. O., Moghalu, O. A., Hatter, S. J., Okunuwadje, S., Anquilano, L., Onwukwe, U., et al. (2022). Clay mineral formation and transformation in non-marine environments and implications for Early Cretaceous palaeoclimatic evolution: The Weald Basin, Southeast England. *Journal of Palaeogeography*, *11*(3), 387–409. https://doi.org/10.1016/j.jop.2022.04.002

Amouric, M., & Olives, J. (1998). Transformation mechanisms and interstratification in conversion of smectite to kaolinite: An HRTEM study. *Clays and Clay Minerals*, *46*(5), 521–527. https://doi.org/10.1346/ccmn.1998.0460505

Beaufort, D., Rigault, C., Billon, S., Billault, V., Inoue, A., Inoué, S., & Patrier, P. (2015). Chlorite and chloritization processes through mixed-layer mineral series in low-temperature geological systems–a review. *Clay Minerals*, *50*(4), 497–523. https://doi.org/10.1180/claymin.2015.050.4.06

Bodden, T. J., Bornhorst, T. J., Bégué, F., & Deering, C. (2022). Sources of hydrothermal fluids inferred from oxygen and carbon isotope composition of calcite, Keweenaw Peninsula Native Copper District, Michigan, USA [Dataset]. *Minerals*, *12*(4), 474. https://doi.org/10.3390/min12040474

Bornhorst, T. J., Paces, J. B., Grant, N. K., Obradovich, J. D., & Huber, N. K. (1988). Age of native copper mineralization, Keweenaw Peninsula, Michigan. *Economic Geology*, *83*(3), 619–625. https://doi.org/10.2113/gsecongeo.83.3.619

Bornhorst, T. J., & Woodruff, L. G. (1997). Native copper precipitation by fluid-mixing Keweenaw Peninsula, Michigan [Dataset]. *Institute on Lake Superior Geology Proceedings*, *4*(Pt 1), 9–10. Retrieved from https://digitalcollections.lakeheadu.ca/exhibits/show/ilsg/item/2919

Brojanigo, A. (1984). Keweenaw Fault: Structures and sedimentology [M.Sc. thesis] (p. 124). Michigan Technological University.

Bunker, B. J., Witzke, B. J., Watney, W. L., & Ludvigson, G. A. (1988). Phanerozoic history of the central midcontinent, United States. In L. L. Sloss (Ed.), *Sedimentary Cover—North American Craton: U.S.* (Vol. D-2, pp. 243–260). Geological Society of America, The Geology of North America. https://doi.org/10.1130/dnag-gna-d2.243

Burbank, D. W., & Raynolds, R. G. (1988). Stratigraphic keys to the timing of thrusting in terrestrial foreland basins: Applications to the northwestern Himalaya. In *New perspectives in basin analysis* (pp. 331–351). Springer New York.

Burov, E. B., & Diament, M. (1995). The effective elastic thickness (Te) of continental lithosphere: What does it really mean? *Journal of Geophysical Research*, *100*(B3), 3905–3927. https://doi.org/10.1029/94jb02770

Burov, E. B., & Poliakov, A. (2003). Erosional forcing of basin dynamics: New aspects of syn-and post-rift evolution. *Geological Society, London, Special Publications*, *212*(1), 209–223. https://doi.org/10.1144/gsl.sp.2003.212.01.14

Byers, C. W., & Dott, R. H. (1995). Sedimentology and depositional sequences of the Jordan Formation (Upper Cambrian), northern Mississippi Valley. *Journal of Sedimentary Research*, *65*(3b), 289–305.

Cannon, W. F. (1992). The Midcontinent rift in the Lake Superior region with emphasis on its geodynamic evolution. *Tectonophysics*, *213*(1–2), 41–48. https://doi.org/10.1016/0040-1951(92)90250-A

Cannon, W. F. (1994). Closing of the Midcontinent Rift—A far-field effect of Grenvillian compression. *Geology*, *22*(2), 155–158. https://doi.org/10.1130/0091-7613(1994)022<0155:COTM-RA>2.3.CO;2

Cannon, W. F., & Nicholson, S. W. (2001). Geologic map of the Keweenaw Peninsula and adjacent area, Michigan. U.S. Geological Survey Map I-2696, scale 1:100,000, 1 sheet, 7 pp. Text. https://doi.org/10.3133/i2696

Cannon, W. F., Peterman, Z. E., & Sims, P. K. (1993). Crustal-scale thrusting and origin of the Montreal River monocline—A 35-km-thick cross section of the Midcontinent Rift in northern Michigan and Wisconsin. *Tectonics*, *12*(3), 728–744. https://doi.org/10.1029/93TC00204

Cardozo, N., & Jordan, T. (2001). Causes of spatially variable tectonic subsidence in the Miocene Bermejo Foreland Basin, Argentina [Software]. *Basin Research*, *13*(3), 335–357. https://doi.org/10.1046/j.0950-091X.2001.00154.x

Cawood, P. A., & Pisarevsky, S. A. (2017). Laurentia-Baltica-Amazonia relations during Rodinia assembly. *Precambrian Research*, *292*, 386–397. https://doi.org/10.1016/j.precamres.2017.01.031

Chandler, V. W., McSwiggen, P. L., Morey, G. B., Hinze, W. J., & Anderson, R. R. (1989). Interpretation of seismic reflection, gravity, and magnetic data across middle Proterozoic Mid-continent Rift system, northwestern Wisconsin, eastern Minnesota, and central Iowa. *AAPG Bulletin*, *73*(3), 261–275. https://doi.org/10.1306/703c9b68-1707-11d7-8645000102c1865d

Chang, H. K., Mackenzie, F. T., & Schoonmaker, J. (1986). Comparisons between the diagenesis of dioctahedral and trioctahedral smectite, Brazilian offshore basins. *Clays and Clay Minerals*, *34*(4), 407–423. https://doi.org/10.1346/ccmn.1986.0340408

Chichester, B., Rychert, C., Harmon, N., Lee, S., Frederiksen, A., & Zhang, H. (2018). Seismic imaging of the North American Midcontinent Rift using S -to- P receiver functions. *Journal of Geophysical Research: Solid Earth*, *123*(9), 7791–7805. https://doi.org/10.1029/2018jb015771

Choi, Y. S., & Simo, J. A. (1998). Ramp facies and sequence stratigraphic models in an epeiric sea: The Upper Ordovician mixed carbonate-siliciclastic Glenwood and Platteville formations, Wisconsin, USA. *Geological Society, London, Special Publications*, *149*(1), 437–456. https://doi.org/10.1144/gsl.sp.1999.149.01.20

Cordani, U. G., Cardona, A., Jimenez, D. M., Liu, D., & Nutman, A. P. (2005). Geochronology of Proterozoic basement inliers in the Colombian Andes: Tectonic history of remnants of a fragmented Grenville belt. *Geological Society, London, Special Publications*, *246*(1), 329–346. https://doi.org/10.1144/gsl.sp.2005.246.01.13

Cornwall, H. R. (1955). Bedrock geology of the Fort Wilkins quadrangle, Michigan. USGS Geologic Quadrangle Map GQ-74, scale 1:24,000.

Cox, S. E., Thomson, S. N., Reiners, P. W., Hemming, S. R., & Van De Flierdt, T. (2010). Extremely low long-term erosion rates around the Gamburtsev Mountains in interior East Antarctica. *Geophysical Research Letters*, *37*(22), L22307. https://doi.org/10.1029/2010GL045106

Craddock, J. P., Konstantinou, A., Vervoort, J. D., Wirth, K. R., Davidson, C., Finley-Blasi, L., et al. (2013). Detrital zircon provenance of the Mesoproterozoic Midcontinent Rift, Lake Superior region, USA. *The Journal of Geology*, *121*(1), 57–73. https://doi.org/10.1086/668635

Craddock, J. P., Malone, D. H., Porter, R., Compton, J., Luczaj, J., Konstantinou, A., et al. (2017). Paleozoic reactivation structures in the Appalachian-Ouachita-Marathon foreland: Far-field deformation across Pangea. *Earth-Science Reviews*, *169*, 1–34. https://doi.org/10.1016/j.earscirev.2017.04.002

Creyts, T. T., Ferraccioli, F., Bell, R. E., Wolovick, M., Corr, H., Rose, K. C., et al. (2014). Freezing of ridges and water networks preserves the Gamburtsev Subglacial Mountains for millions of years. *Geophysical Research Letters*, *41*(22), 8114–8122. https://doi.org/10.1002/2014gl061491

Currie, B. S. (2002). Structural configuration of the Early Cretaceous Cordilleran foreland-basin system and Sevier thrust belt, Utah and Colorado. *The Journal of Geology*, *110*(6), 697–718. https://doi.org/10.1086/342626

Daniels, P. A., Jr. (1982). *Upper Precambrian sedimentary rocks* (pp. 107–133). Oronto Group, Michigan-Wisconsin. See Wold & Hinze 1982.

Davis, D. W., & Paces, J. B. (1990). Time resolution of geologic events on the Keweenaw Peninsula and implications for development of the Midcontinent Rift system. *Earth and Planetary Science Letters*, *97*(1–2), 54–64. https://doi.org/10.1016/0012-821x(90)90098-i

DeGraff, J. M., & Carter, B. T. (2023). Detached structural model of the Keweenaw fault system, Lake Superior region, North America: Implications for its origin and relationship to the Midcontinent Rift System. *GSA Bulletin*, *135*(1–2), 449–466. https://doi.org/10.1130/b36186.1

Dehler, C., Schmitz, M., Bullard, A., Porter, S., Timmons, M., Karlstrom, K., & Cothren, H. (2023). Precise U-Pb age models refine Neoproterozoic western Laurentian rift initiation, correlation, and Earth system changes. *Precambrian Research*, *396*, 107156. https://doi.org/10.1016/j.precamres.2023.107156

Dypvik, H. (1983). Clay mineral transformations in Tertiary and Mesozoic sediments from North Sea [Dataset]. *AAPG Bulletin*, *67*(1), 160–165. https://doi.org/10.1306/03B5ACDC-16D1-11D7-8645000102C1865D

Eberl, D. D., Środoń, J., & Northrop, R. (1986). Potassium fixation in smectite by wetting and drying. In J. A. Davis & K. F. Hayes (Eds.), *Geochemical processes at mineral surfaces, ACS Symposium Series 323* (pp. 296–326). American Chemical Society.

Ebinger, C. J., Bechtel, T. D., Forsyth, D. W., & Bowin, C. O. (1989). Effective elastic plate thicknesses beneath the East African and Afar domes. *Journal of Geophysical Research*, *94*, 2883–2990.

Eddy, M. P., Bowring, S. A., Umhoefer, P. J., Miller, R. B., McLean, N. M., & Donaghy, E. E. (2016). High-resolution temporal and stratigraphic record of Siletzia's accretion and triple junction migration from nonmarine sedimentary basins in central and western Washington. *Bulletin*, *128*(3–4), 425–441. https://doi.org/10.1130/b31335.1

Eoff, J. D. (2014). Sequence stratigraphy of the Upper Cambrian (Furongian; Jiangshanian and Sunwaptan) Tunnel City Group, Upper Mississippi Valley: Transgressing assumptions of cratonic flooding. *Sedimentary Geology*, *302*, 87–101. https://doi.org/10.1016/j.sedgeo.2013.09.007

Fairchild, L. M., Swanson-Hysell, N. L., Ramezani, J., Sprain, C. J., & Bowring, S. A. (2017). The end of Midcontinent Rift magmatism and the paleogeography of Laurentia. *Lithosphere*, *9*(1), 117–133. https://doi.org/10.1130/l580.1

Farley, K. A., & McKeon, R. (2015). Radiometric dating and temperature history of banded iron formation–associated hematite, Gogebic iron range, Michigan, USA [Dataset]. *Geology*, *43*(12), 1083–1086. https://doi.org/10.1130/G37190.1

Fedo, C. M., Sircombe, K. N., & Rainbird, R. H. (2003). Detrital zircon analysis of the sedimentary record. *Reviews in Mineralogy and Geochemistry*, *53*(1), 277–303. https://doi.org/10.2113/0530277

Fisher, G. B., & Ryan, P. C. (2006). The smectite-to-disordered kaolinite transition in a tropical soil chronosequence, Pacific Coast, Costa Rica. *Clays and Clay Minerals*, *54*(5), 571–586. https://doi.org/10.1346/ccmn.2006.0540504

Flowers, R. M., Ketcham, R. A., Macdonald, F. A., Siddoway, C. S., & Havranek, R. E. (2022). Existing thermochronologic data do not constrain Snowball glacial erosion below the Great Unconformities. *Proceedings of the National Academy of Sciences*, *119*(38), e2208451119. https://doi.org/10.1073/pnas.2208451119

Flowers, R. M., Macdonald, F. A., Siddoway, C. S., & Havranek, R. (2020). Diachronous development of Great Unconformities before Neoproterozoic Snowball Earth. *Proceedings of the National Academy of Sciences*, *117*(19), 10172–10180. https://doi.org/10.1073/pnas.1913131117

Freiburg, J. T., Amer, M., Henkel, K., Wemmer, K., & Grathoff, G. H. (2022). Illitization in the Mt. Simon Sandstone, Illinois Basin, USA: Implications for carbon dioxide storage. *Marine and Petroleum Geology*, *146*, 105963. https://doi.org/10.1016/j.marpetgeo.2022.105963

Gair, J. E., & Thaden, R. E. (1968). Geology of the Marquette and Sands quadrangles, Marquette County, MI (p. 77). U.S. Geol. Sur. Prof. paper 397.

Gallagher, B., & Bjornerud, M. (2021). Reconstructing the hydration and carbonation history of the Presque Isle peridotite, Marquette Michigan: Insights into mechanisms of carbon sequestration in ultramafic rocks. Institute of Lake Superior Geology [abs.]: Institute on Lake Superior Geology. *Proceedings, 67th Annual Meeting*, *67*(1), 26–27. ISSN 1042-99.

Gallagher, T. M., Sheldon, N. D., Mauk, J. L., Petersen, S. V., Gueneli, N., & Brocks, J. J. (2017). Constraining the thermal history of the North American Midcontinent Rift System using carbonate clumped isotopes and organic thermal maturity indices [Dataset]. *Precambrian Research*, *294*, 53–66. https://doi.org/10.1016/j.precamres.2017.03.022

Garcia-Castellanos, D., & Cloetingh, S. I. E. R. D. (2011). Modeling the interaction between lithospheric and surface processes in foreland basins. In *Tectonics of sedimentary basins: Recent advances* (pp. 152–181).

Gerasimov, S. H., Hodgin, E. B., Crowley, J. L., & Swanson-Hysell, N. L. (2024). Chronostratigraphy of Miocene strata in the Berkeley Hills (California Coast Ranges, USA) and the arrival of the San Andreas transform boundary. *Geosphere*, *20*(1), 162–178. https://doi.org/10.1130/GES02650.1

Ghosh, P., Adkins, J., Affek, H., Balta, B., Guo, W., Schauble, E. A., et al. (2006). ^{13}C-^{18}O bonds in carbonate minerals: A new kind of paleothermometer. *Geochimica et Cosmochimica Acta*, *70*(6), 1439–1456. https://doi.org/10.1016/j.gca.2005.11.014

Goddéris, Y., Le Hir, G., & Donnadieu, Y. (2011). Modelling the snowball Earth. In E. Arnaud, G. P. Halverson, & G. Shields-Zhou (Eds.), *The geological record of Neoproterozoic glaciations* (Vol. 36, pp. 151–161). Geological Society, London.

Grant, U. S. (1901). Preliminary report on the copper-bearing rocks of Douglas County, Wisconsin. (No. 3). State.

Grathoff, G. H., Moore, D. M., Hay, R. L., & Wemmer, K. (2001). Origin of illite in the lower Paleozoic of the Illinois basin: Evidence for brine migrations. *Geological Society of America Bulletin*, *113*(8), 1092–1104. https://doi.org/10.1130/0016-7606(2001)113<1092:ooiitl>2.0.co;2

Greenman, J. W., Rooney, A. D., Patzke, M., Ielpi, A., & Halverson, G. P. (2021). Re-Os geochronology highlights widespread latest Mesoproterozoic (ca. 1090–1050 Ma) cratonic basin development on northern Laurentia. *Geology*, *49*(7), 779–783. https://doi.org/10.1130/G48521.1

Hamblin, W. K. (1958). *The Cambrian sandstones of northern Michigan* (Vol. 51). University of Michigan.

Hantsche, A., Farmer, G. L., Espinoza Maldonado, I. G., Fedo, C. M., & Siddoway, C. (2021). U-Pb and Hf isotopic evidence on the sources and sinks of Grenvillian detrital zircons in early Laurentia. *The Journal of Geology*, *129*(6), 673–693. https://doi.org/10.1086/716965

Hatcher, R. D., Jr., Thomas, W. A., Geiser, P. A., Snoke, A. W., Mosher, S., & Wiltschko, D. V. (1989). Alleghanian orogen. In *The Appalachian-Ouachita Orogen in the United States* (Vol. 2, pp. 233–318). Geological Society of America, The Geology of North America.

Hedgman, C. (1992). Provenance and tectonic setting of the Jacobsville Sandstone, from Ironwood to Keweenaw Bay, Michigan [M.Sc. thesis] (p. 158). University of Cincinnati.

Heine, C., Müller, R. D., Steinberger, B., & Torsvik, T. H. (2008). Subsidence in intracontinental basins due to dynamic topography. *Physics of the Earth and Planetary Interiors*, *171*(1–4), 252–264. https://doi.org/10.1016/j.pepi.2008.05.008

Herriott, T. M., Crowley, J. L., Schmitz, M. D., Wartes, M. A., & Gillis, R. J. (2019). Exploring the law of detrital zircon: LA-ICP-MS and CA-TIMS geochronology of Jurassic forearc strata, Cook Inlet, Alaska, USA. *Geology*, *47*(11), 1044–1048. https://doi.org/10.1130/G46312.1

Hite, D. M. (1968). Sedimentology of the upper Keweenawan sequence of northern Wisconsin and adjacent Michigan [Ph.D. thesis] (p. 217). University of Wisconsin, Madison.

Hodgin, E. B., Carlotto, V., Macdonald, F. A., Schmitz, M. D., & Crowley, J. L. (2023). New age constraints on the break-up of Rodinia and amalgamation of southwestern Gondwana from the Choquequirao Formation in southwestern Peru. *Geological Society, London, Special Publications*, *531*(1), 301–321. https://doi.org/10.1144/SP531-2022-197

Hodgin, E. B., Macdonald, F. A., Karabinos, P., Crowley, J. L., & Reusch, D. N. (2022). A reevaluation of the tectonic history of the Dashwoods terrane using in situ and isotope-dilution U-Pb geochronology, western Newfoundland. In Y. D. Kuiper, J. B. Murphy, R. D. Nance, R. A.

Strachan, & M. D. Thompson (Eds.), *New developments in the Appalachian-Caledonian-Variscan Orogen*, *Geological Society of America Special Paper 554* (pp. 243–264). https://doi.org/10.1130/2021.2554(10)

Hodgin, E. B., Swanson-Hysell, N. L., DeGraff, J. M., Kylander-Clark, A. R., Schmitz, M. D., Turner, A. C., et al. (2022). Final inversion of the Midcontinent Rift during the Rigolet Phase of the Grenvillian Orogeny [Dataset]. *Geology*, *50*(5), 547–551. https://doi.org/10.1130/g49439.1

Hoffman, P. F. (2023). Glacial erosion on a snowball Earth: Testing for bias in flux balance, geographic setting, and tectonic regime. *Canadian Journal of Earth Sciences*, *60*(7), 765–777. https://doi.org/10.1139/cjes-2022-0004

Hoffman, P. F., Abbot, D. S., Ashkenazy, Y., Benn, D. I., Brocks, J. J., Cohen, P. A., et al. (2017). Snowball Earth climate dynamics and Cryogenian geology-geobiology. *Science Advances*, *3*(11), e1600983. https://doi.org/10.1126/sciadv.1600983

Holland, M. E., Mohr, M., Schmitz, M., Madronich, L., & Karlstrom, K. (2024). Source-to-sink tandem geochronology reveals tectonic influences on the Cambrian Transcontinental Arch of Laurentia. *Terra Nova*, *36*(2), 161–169. https://doi.org/10.1111/ter.12692

Horton, B. K., Capaldi, T. N., Mackaman-Lofland, C., Perez, N. D., Bush, M. A., Fuentes, F., & Constenius, K. N. (2022). Broken foreland basins and the influence of subduction dynamics, tectonic inheritance, and mechanical triggers. *Earth-Science Reviews*, *234*, 104193. https://doi.org/10.1016/j.earscirev.2022.104193

Horton, B. K., & DeCelles, P. G. (1997). The modern foreland basin system adjacent to the Central Andes. *Geology*, *25*(10), 895–898. https://doi.org/10.1130/0091-7613(1997)025<0895:tmfbsa>2.3.co;2

Howard, A. L., Farmer, G. L., Amato, J. M., & Fedo, C. M. (2015). Zircon U–Pb ages and Hf isotopic compositions indicate multiple sources for Grenvillian detrital zircon deposited in western Laurentia. *Earth and Planetary Science Letters*, *432*, 300–310. https://doi.org/10.1016/j.epsl.2015.10.018

Huntington, K. W., & Petersen, S. V. (2023). Frontiers of carbonate clumped isotope thermometry. *Annual Review of Earth and Planetary Sciences*, *51*(1), 611–641. https://doi.org/10.1146/annurev-earth-031621-085949

Huyghe, P., Guilbaud, R., Bernet, M., Galy, A., & Gajurel, A. P. (2011). Significance of the clay mineral distribution in fluvial sediments of the Neogene to Recent Himalayan Foreland Basin (west-central Nepal). *Basin Research*, *23*(3), 332–345. https://doi.org/10.1111/j.1365-2117.2010.00485.x

Hynes, A., & Rivers, T. (2010). Protracted continental collision—Evidence from the Grenville Orogen. *Canadian Journal of Earth Sciences*, *47*(5), 591–620. https://doi.org/10.1139/E10-003

Ibarra, D. E., Kukla, T., Methner, K. A., Mulch, A., & Chamberlain, C. P. (2021). Reconstructing past elevations from triple oxygen isotopes of lacustrine chert: Application to the Eocene Nevadaplano, Elko Basin, Nevada, United States. *Frontiers in Earth Science*, *9*, 628868. https://doi.org/10.3389/feart.2021.628868

Ielpi, A., & Rainbird, R. H. (2016). Highly variable Precambrian fluvial style recorded in the Nelson Head Formation of Brock Inlier (Northwest Territories, Canada). *Journal of Sedimentary Research*, *86*(3), 199–216. https://doi.org/10.2110/jsr.2016.16

Isakson, V. H., Schmitz, M. D., Dehler, C. M., Macdonald, F. A., & Yonkee, W. A. (2022). A robust age model for the Cryogenian Pocatello Formation of southeastern Idaho (northwestern USA) from tandem in situ and isotope dilution U-Pb dating of volcanic tuffs and epiclastic detrital zircons. *Geosphere*, *18*(2), 825–849. https://doi.org/10.1130/GES02437.1

Jaffey, A. H., Flynn, K. F., Glendenin, L. E., Bentley, W. T., & Essling, A. M. (1971). Precision measurement of half-lives and specific activities of U 235 and U 238. *Physical Review C*, *4*(5), 1889–1906. https://doi.org/10.1103/physrevc.4.1889

Jamieson, S. S., Sugden, D. E., & Hulton, N. R. (2010). The evolution of the subglacial landscape of Antarctica. *Earth and Planetary Science Letters*, *293*(1–2), 1–27. https://doi.org/10.1016/j.epsl.2010.02.012

Jautzy, J. J., Savard, M. M., Dhillon, R. S., Bernasconi, S. M., & Smirnoff, A. (2020). Clumped isotope temperature calibration for calcite: Bridging theory and experimentation. *Geochemical Perspectives Letters*, *14*, 36–41. https://doi.org/10.7185/geochemlet.2021

Jirsa, M. A., Boerboom, T. J., Chandler, V. W., Mossler, J. H., Runkel, A. C., & Setterholm, D. R. (2011). Geologic map of Minnesota: Bedrock geology. Minnesota Geological Survey State Map 21, scale 1:500,000 [Dataset]. Retrieved from http://hdl.handle.net/11299/101466

Kalliokoski, J. (1975). Chemistry and mineralogy of Precambrian paleosols in northern Michigan. *Geological Society of America Bulletin*, *86*(3), 371–376. https://doi.org/10.1130/0016-7606(1975)86<371:camopp>2.0.co;2

Kalliokoski, J. (1976). *Uranium and thorium occurrences in Precambrian rocks, Upper Peninsula of Michigan and Northern Wisconsin; with thoughts on other possible settings*. U.S. Energy Research and Development Administration.

Kalliokoski, J. (1982). Jacobsville sandstone. In R. J. Wold & W. J. Hinze (Eds.), *Geology and tectonics of the Lake Superior Basin*, *Geol. Soc. Am. Memoir* (Vol. 156, pp. 147–155).

Karlstrom, K. E., Mohr, M. T., Schmitz, M. D., Sundberg, F. A., Rowland, S. M., Blakey, R., et al. (2020). Redefining the Tonto Group of Grand Canyon and recalibrating the Cambrian time scale. *Geology*, *48*(5), 425–430. https://doi.org/10.1130/G46755.1

Keller, C. B., Husson, J. M., Mitchell, R. N., Bottke, W. F., Gernon, T. M., Boehnke, P., et al. (2019). Neoproterozoic glacial origin of the Great Unconformity. *Proceedings of the National Academy of Sciences*, *116*(4), 1136–1145. https://doi.org/10.1073/pnas.1804350116

Keppie, J. D., & Ortega-Gutiérrez, F. (2010). 1.3–0.9 Ga Oaxaquia (Mexico): Remnant of an arc/backarc on the northern margin of Amazonia. *Journal of South American Earth Sciences*, *29*(1), 21–27. https://doi.org/10.1016/j.jsames.2009.07.001

Krogh, T. E. (1994). Precise U-Pb ages for Grenvillian and pre-Grenvillian thrusting of Proterozoic and Archean metamorphic assemblages in the Grenville Front tectonic zone, Canada. *Tectonics*, *13*(4), 963–982. https://doi.org/10.1029/94TC00801

Lanson, B., Beaufort, D., Berger, G., Bauer, A., Cassagnabere, A., & Meunier, A. (2002). Authigenic kaolin and illitic minerals during burial diagenesis of sandstones: A review. *Clay Minerals*, *37*(1), 1–22. https://doi.org/10.1180/0009855023710014

Lewan, M. D. (1972). Metasomatism and weathering of the Presque Isle serpentinized peridotite, Marquette, Michigan [MSc. thesis] (p. 48). Michigan Technological University.

Li, Z., & Aschoff, J. (2022). Constraining the effects of dynamic topography on the development of Late Cretaceous Cordilleran foreland basin, western United States. *GSA Bulletin*, *134*(1–2), 446–462. https://doi.org/10.1130/b35838.1

Livnat, A. (1983). Metamorphism and copper mineralization of the Portage Lake Lava Series, Northern Michigan [Ph.D. thesis] (pp. 1–292). University of Michigan.

Lochman-Balk, C., & Holland, C. H. (1971). The Cambrian of the craton of the United States. In *Cambrian of the New World* (pp. 79–168). Wiley Interscience.

Looser, N., Madritsch, H., Guillong, M., Laurent, O., Wohlwend, S., & Bernasconi, S. M. (2021). Absolute age and temperature constraints on deformation along the basal décollement of the Jura fold-and-thrust belt from carbonate U-Pb dating and clumped isotopes. *Tectonics*, *40*(3), e2020TC006439. https://doi.org/10.1029/2020tc006439

Ludwig, K. R. (1998). On the treatment of concordant uranium-lead ages. *Geochimica et Cosmochimica Acta*, *62*(4), 665–676. https://doi.org/10.1016/s0016-7037(98)00059-3

Mangenot, X., Gasparrini, M., Gerdes, A., Bonifacie, M., & Rouchon, V. (2018). An emerging thermochronometer for carbonate-bearing rocks: Δ_{47}/(U-Pb). *Geology*, *46*(12), 1067–1070. https://doi.org/10.1130/g45196.1

Mauk, J. L., Brown, A. C., Seasor, R. W., & Eldridge, C. S. (1992). Geology and stable isotope and organic geochemistry of the White Pine sediment-hosted stratiform copper deposit [Dataset]. *Society of Economic Geologists Guidebook Series*, *13*, 63–98. https://doi.org/10.5382/gb.13.03

Mauk, J. L., & Hieshima, G. B. (1992). Organic matter and copper mineralization at White Pine, Michigan, USA. *Chemical Geology*, *99*(1–3), 189–211. https://doi.org/10.1016/0009-2541(92)90038-7

McCabe, C., & Van Der Voo, R. (1983). Paleomagnetic results from the upper Keweenawan Chequamegon Sandstone: Implications for red bed diagenesis and Late Precambrian apparent polar wander of North America. *Canadian Journal of Earth Sciences*, *20*(1), 105–112. https://doi.org/10.1139/e83-010

McDannell, K. T., Keller, C. B., Guenthner, W. R., Zeitler, P. K., & Shuster, D. L. (2022). Thermochronologic constraints on the origin of the Great Unconformity. *Proceedings of the National Academy of Sciences*, *119*(5), e2118682119. https://doi.org/10.1073/pnas.2118682119

Milstein, R. L. (1987). Anomalous Paleozoic outliers near Limestone Mountain, Michigan. In D. L. Biggs (Ed.), *North Central section of the Geological Society of America*, *Centennial field guide* (Vol. 3, pp. 263–268). Geological Society of America. https://doi.org/10.1130/0-8137-5403-8.263

Mitrovica, J. X., Beaumont, C., & Jarvis, G. T. (1989). Tilting of continental interiors by the dynamical effects of subduction. *Tectonics*, *8*(5), 1079–1094. https://doi.org/10.1029/tc008i005p01079

Morey, G. B. (2001). Compositions of rift-related volcanic rocks of the Keweenawan Supergroup atop the St. Croix horst, southeastern Minnesota. In *Minnesota Geological Survey Information Circular* (Vol. 47, p. 27).

Morey, G. B., & Ojakangas, R. W. (1982). Keweenawan sedimentary rocks of eastern Minnesota and northwestern Wisconsin. In R. J. Wold & W. J. Hinze (Eds.), *Geology and tectonics of the Lake Superior Basin*, *Mem. Geol. Soc. Am.* (Vol. 156, pp. 135–146).

Mossler, J. H. (2008). *RI-65 Paleozoic stratigraphic nomenclature for Minnesota*. Minnesota Geological Survey. University of Minnesota Digital Conservancy. Retrieved from https://hdl.handle.net/11299/58940

Myers, W. D. (1971). The sedimentology and tectonic significance of the Bayfield Group (upper Keweenawan?) Wisconsin and Minnesota [Ph.D. thesis] [Dataset]. *University of Wisconsin–Madison*, 269. Retrieved fromhttps://www.proquest.com/docview/302615256?fromopenview=true&pq-origsite=gscholar&sourcetype=Dissertations%20&%20Theses

Naylor, S., Wickert, A. D., Edmonds, D. A., & Yanites, B. J. (2021). Landscape evolution under the southern Laurentide Ice Sheet. *Science Advances*, *7*(48), eabj2938. https://doi.org/10.1126/sciadv.abj2938

Neil, B. J., Gibson, H. D., Pehrsson, S. J., Martel, E., Thiessen, E. J., & Crowley, J. L. (2021). Provenance, stratigraphic and precise depositional age constraints for an outlier of the 1.9 to 1.8 Ga Nonacho Group, Rae craton, Northwest Territories, Canada. *Precambrian Research*, *352*, 105999. https://doi.org/10.1016/j.precamres.2020.105999

Nelson, L. L., Crowley, J. L., Smith, E. F., Schwartz, D. M., Hodgin, E. B., & Schmitz, M. D. (2023). Cambrian explosion condensed: High-precision geochronology of the lower Wood Canyon Formation, Nevada. *Proceedings of the National Academy of Sciences*, *120*(30), e2301478120. https://doi.org/10.1073/pnas.2301478120

Nicholson, S. W., Cannon, W. F., Woodruff, L. G., & Dicken, C. (2006). *Bedrock geologic map of the Port Wing, Solon Springs, and parts of the Duluth and Sandstone 30'X 60'quadrangles, Wisconsin* (Scientific Investigations Map 2869). US Geological Survey.

Nicholson, S. W., Dicken, C. L., Foose, M. P., & Mueller, J. (2004). Integrated geologic map databases for the United States; the Upper Midwest States: Minnesota, Wisconsin, Michigan, Illinois, and Indiana (Tech. Rep.) [Dataset]. *US Geological Survey*. https://doi.org/10.3133/ofr20041355

Nishioka, G. K. (1983). *Origin of late veins in the White Pine copper deposit, northern Michigan* [M.S. thesis]. University of Michigan.

Ojakangas, R. W., Morey, G. B., & Green, E. C. (2001). The Mesoproterozoic Midcontinent Rift system, Lake Superior region, USA. *Sedimentary Geology*, *141*, 421–442. https://doi.org/10.1016/S0037-0738(01)00085-9

Oravecz, É., Balázs, A., Gerya, T., May, D. A., & Fodor, L. (2024). Competing effects of crustal shortening, thermal inheritance, and surface processes explain subsidence anomalies in inverted rift basins. *Geology*, *52*(6), 447–452. https://doi.org/10.1130/G51971.1

Passey, B. H., & Henkes, G. A. (2012). Carbonate clumped isotope bond reordering and geospeedometry. *Earth and Planetary Science Letters*, *351*, 223–236. https://doi.org/10.1016/j.epsl.2012.07.021

Peak, B. A., Flowers, R. M., & Macdonald, F. A. (2023). Ediacaran-Ordovician tectonic and geodynamic drivers of Great Unconformity exhumation on the southern Canadian Shield [Dataset]. *Earth and Planetary Science Letters*, *619*, 118334. https://doi.org/10.1016/j.epsl.2023.118334

Peppers, R. A. (1996). *Palynological correlation of major Pennsylvanian (Middle and Upper Carboniferous) chronostratigraphic boundaries in the Illinois and other coal basins* (Vol. 188). Geological Society of America. https://doi.org/10.1130/0-8137-1188-6.1

Perrot, M., Tremblay, A., & David, J. (2017). Detrital zircon U-Pb geochronology of the Magog Group, southern Quebec – Stratigraphic and tectonic implications for the Quebec Appalachians. *American Journal of Science*, *317*(10), 1049–1094. https://doi.org/10.2475/10.2017.01

Pett-Ridge, J. C., Monastra, V. M., Derry, L. A., & Chadwick, O. A. (2007). Importance of atmospheric inputs and Fe-oxides in controlling soil uranium budgets and behavior along a Hawaiian chronosequence. *Chemical Geology*, *244*(3–4), 691–707. https://doi.org/10.1016/j.chemgeo.2007.07.016

Pierrehumbert, R. T., Abbot, D. S., Voigt, A., & Koll, D. (2011). Climate of the Neoproterozoic. *Annual Review of Earth and Planetary Sciences*, *39*(1), 417–460. https://doi.org/10.1146/annurev-earth-040809-152447

Pinet, N. (2016). Far-field effects of Appalachian orogenesis: A view from the craton. *Geology*, *44*(2), 83–86. https://doi.org/10.1130/g37356.1

Price, K. L., & McDowell, S. D. (1993). Illite/smectite geothermometry of the Proterozoic Oronto Group, midcontinent rift system. *Clays and Clay Minerals*, *41*(2), 134–147. https://doi.org/10.1346/ccmn.1993.0410203

Rainbird, R. H., Cawood, P., & Gehrels, G. (2011). The great Grenvillian sedimentation episode: Record of supercontinent Rodinia's assembly. In *Tectonics of sedimentary basins: Recent advances* (pp. 583–601).

Rainbird, R. H., Hearnan, L. M., & Young, G. (1992). Sampling Laurentia: Detrital zircon geochronology offers evidence for an extensive Neoproterozoic river system originating from the Grenville orogen. *Geology*, *20*(4), 351–354. https://doi.org/10.1130/0091-7613(1992)020<0351:sldzgo>2.3.co;2

Rainbird, R. H., Rayner, N. M., Hadlari, T., Heaman, L. M., Ielpi, A., Turner, E. C., & MacNaughton, R. B. (2017). Zircon provenance data record the lateral extent of pancontinental, early Neoproterozoic rivers and erosional unroofing history of the Grenville orogen. *Bulletin*, *129*(11–12), 1408–1423. https://doi.org/10.1130/b31695.1

Ramos, V. A. (2010). The Grenville-age basement of the Andes. *Journal of South American Earth Sciences*, *29*(1), 77–91. https://doi.org/10.1016/j.jsames.2009.09.004

Ramsay, J. G. (1980). The crack–seal mechanism of rock deformation. *Nature*, *284*(5752), 135–139. https://doi.org/10.1038/284135a0

Rayner, N. M., & Rainbird, R. H. (2013). U-Pb geochronology of the Shaler Supergroup, Victoria Island, northwest Canada: 2009–2013. Geological Survey of Canada Open File, 7419 (p. 62).

Rivers, T., Culshaw, N., Hynes, A., Indares, A., Jamieson, R., & Martignole, J. (2012). The Grenville Orogen — A post-LITHOPROBE perspective. In J. A. Percival, F. A. Cook, & R. M. Clowes (Eds.), *Tectonic styles in Canada: The LITHOPROBE perspective* (pp. 97–236). Geological Association of Canada, Special Paper 49. Chapter 3.

Roark, A., Flake, R., Grossman, E. L., Olszewski, T., Lebold, J., Thomas, D., et al. (2017). Brachiopod geochemical records from across the Carboniferous seas of North America: Evidence for salinity gradients, stratification, and circulation patterns. *Palaeogeography, Palaeoclimatology, Palaeoecology*, *485*, 136–153. https://doi.org/10.1016/j.palaeo.2017.06.009

Ruiz, J., Jones, L. M., & Kelly, W. C. (1984). Rubidium-strontium dating of ore deposits hosted by Rb-rich rocks, using calcite and other common Sr-bearing minerals. *Geology*, *12*(5), 259–262. https://doi.org/10.1130/0091-7613(1984)12<259:RDOO-DH>2.0.CO;2

Runkel, A. C., Miller, J. F., McKay, R. M., Palmer, A. R., & Taylor, J. F. (2007). High-resolution sequence stratigraphy of lower Paleozoic sheet sandstones in central North America: The role of special conditions of cratonic interiors in development of stratal architecture. *Geological Society of America Bulletin*, *119*(7–8), 860–881. https://doi.org/10.1130/b26117.1

Sak, P. B., Fisher, D. M., Gardner, T. W., Murphy, K., & Brantley, S. L. (2004). Rates of weathering rind formation on Costa Rican basalt. *Geochimica et Cosmochimica Acta*, *68*(7), 1453–1472. https://doi.org/10.1016/j.gca.2003.09.007

Salem, A. M., Morad, S., Mato, L. F., & Al-Aasm, I. S. (2000). Diagenesis and reservoir-quality evolution of fluvial sandstones during progressive burial and uplift: Evidence from the Upper Jurassic Boipeba Member, Recôncavo Basin, Northeastern Brazil. *AAPG Bulletin*, *84*(7), 1015–1040. https://doi.org/10.1306/a9673b9e-1738-11d7-8645000102c1865d

Sandiford, M., & Powell, R. (1986). Deep crustal metamorphism during continental extension: Modern and ancient examples. *Earth and Planetary Science Letters*, *79*(1–2), 151–158. https://doi.org/10.1016/0012-821x(86)90048-8

Setterholm, D. R. (2010). C-22 Geologic Atlas of Chisago County, Minnesota [Part A].

Sharman, G. R., & Malkowski, M. A. (2020). Needles in a haystack: Detrital zircon UPb ages and the maximum depositional age of modern global sediment. *Earth-Science Reviews*, *203*, 103109. https://doi.org/10.1016/j.earscirev.2020.103109

Sharp, Z. D., Gibbons, J. A., Maltsev, O., Atudorei, V., Pack, A., Sengupta, S., et al. (2016). A calibration of the triple oxygen isotope fractionation in the SiO_2–H_2O system and applications to natural samples. *Geochimica et Cosmochimica Acta*, *186*, 105–119. https://doi.org/10.1016/j.gca.2016.04.047

Sloss, L. L. (1963). Sequences in the cratonic interior of North America. *Geological Society of America Bulletin*, *74*(2), 93–114. https://doi.org/10.1130/0016-7606(1963)74[93:sitcio]2.0.co;2

Slotznick, S. P., Swanson-Hysell, N. L., Zhang, Y., Clayton, K. E., Wellman, C. H., Tosca, N. J., & Strother, P. K. (2024). Reconstructing the paleoenvironment of an oxygenated Mesoproterozoic shoreline and its record of life. *GSA Bulletin*, *136*(3–4), 1628–1650. https://doi.org/10.1130/B36634.1

Smith, K. L., Milnes, A. R., & Eggleton, R. A. (1987). Weathering of basalt: Formation of iddingsite. *Clays and Clay Minerals*, *35*(6), 418–428. https://doi.org/10.1346/CCMN.1987.0350602

Solari, L. A., Keppie, J. D., Ortega-Gutiérrez, F., Cameron, K. L., Lopez, R., & Hames, W. E. (2003). 990 and 1100 Ma Grenvillian tectonothermal events in the northern Oaxacan Complex, southern Mexico: Roots of an orogen. *Tectonophysics*, *365*(1–4), 257–282. https://doi.org/10.1016/s0040-1951(03)00025-8

Song, T., & Wang, X. (1993). Structural styles and stratigraphic patterns of syndepositional faults in a contractional setting: Examples from Quaidam Basin, Northwestern China. *AAPG Bulletin*, *77*(1), 102–117. https://doi.org/10.1306/bdff8b78-1718-11d7-8645000102c1865d

Środoń, J. (1999). Nature of mixed-layer clays and mechanisms of their formation and alteration. *Annual Review of Earth and Planetary Sciences*, *27*(1), 19–53. https://doi.org/10.1146/annurev.earth.27.1.19

Środoń, J., & Eberl, D. D. (1984). Illite. In S. W. Bailey (Ed.), *Micas*, *Reviews in mineralogy* (Vol. 13, pp. 495–544).

Stewart, E. K., Bauer, A. M., & Prave, A. R. (2023). End-Mesoproterozoic (ca. 1.08 Ga) epeiric seaway of the Nonesuch Formation, Wisconsin and Michigan, USA. *Geological Society of America Bulletin*, *136*(7–8), 2940–2960. https://doi.org/10.1130/B37060.1

Stolper, D. A., & Eiler, J. M. (2015). The kinetics of solid-state isotope-exchange reactions for clumped isotopes: A study of inorganic calcites and apatites from natural and experimental samples. *American Journal of Science*, *315*(5), 363–411. https://doi.org/10.2475/05.2015.01

Strecker, M. R., Hilley, G. E., Bookhagen, B., & Sobel, E. R. (2011). Structural, geomorphic, and depositional characteristics of contiguous and broken foreland basins: Examples from the eastern flanks of the central Andes in Bolivia and NW Argentina. In *Tectonics of sedimentary basins: Recent advances* (pp. 508–521).

Sturrock, C. P., Flowers, R. M., Kohn, B. P., & Metcalf, J. R. (2024). Phanerozoic burial and erosion history of the Southern Canadian Shield from apatite (U-Th)/He thermochronology. *Minerals*, *14*(1), 57. https://doi.org/10.3390/min14010057

Sturrock, C. P., Flowers, R. M., & Macdonald, F. A. (2021). The late Great Unconformity of the Central Canadian Shield [Dataset]. *Geochemistry, Geophysics, Geosystems*, *22*(6), e2020GC009567. https://doi.org/10.1029/2020GC009567

Suarez, S. E., Brookfield, M. E., Catlos, E. J., & Stöckli, D. F. (2017). A U-Pb zircon age constraint on the oldest-recorded air-breathing land animal. *PLoS One*, *12*(6), e0179262. https://doi.org/10.1371/journal.pone.0179262

Suppe, J., & Medwedeff, D. A. (1990). Geometry and kinematics of fault-propagation folding. *Eclogae Geologicae Helvetiae*, *83*(3), 409–454.

Swanson-Hysell, N. L., & Macdonald, F. A. (2017). Tropical weathering of the Taconic orogeny as a driver for Ordovician cooling. *Geology*, *45*(8), 719–722.

Swanson-Hysell, N. L., Ramezani, J., Fairchild, L. M., & Rose, I. R. (2019). Failed rifting and fast drifting: Midcontinent Rift development, Laurentia's rapid motion and the driver of Grenvillian oro-genesis. *Geological Society of America Bulletin*, *131*(5–6), 913–940. https://doi.org/10.1130/B31944.1

Swanson-Hysell, N. L., Rivers, T., & van der Lee, S. (2023). The late Mesoproterozoic to early Neoproterozoic Grenvillian orogeny and the assembly of Rodinia: Turning point in the tectonic evolution of Laurentia. https://doi.org/10.1130/2022.1220(14)

Thwaites, F. T. (1912). Sandstones of the Wisconsin coast of Lake Superior. *Wisconsin Geological and Natural History Survey Bulletin*, *25*, 117.

van Acken, D., Thomson, D., Rainbird, R. H., & Creaser, R. A. (2013). Constraining the depositional history of the Neoproterozoic Shaler Supergroup, Amundsen Basin, NW Canada: Rhenium-osmium dating of black shales from the Wynniatt and Boot Inlet Formations. *Precambrian Research*, *236*, 124–131. https://doi.org/10.1016/j.precamres.2013.07.012

Van Schmus, W. R., & Hinze, W. J. (1985). The Midcontinent Rift system. *Annual Review of Earth and Planetary Sciences*, *13*(1), 345–383. https://doi.org/10.1146/annurev.ea.13.050185.002021

Vermeesch, P. (2018). IsoplotR: A free and open toolbox for geochronology [Software]. *Geoscience Frontiers*, *9*(5), 1479–1493. https://doi.org/10.1016/j.gsf.2018.04.001

Voigt, A. (2013). The dynamics of the snowball earth Hadley circulation for off-equatorial and seasonally varying insolation. *Earth System Dynamics*, *4*(2), 425–438. https://doi.org/10.5194/esd-4-425-2013

Weibel, R. (1999). Effects of burial on the clay assemblages in the Triassic Skagerrak Formation, Denmark. *Clay Minerals*, *34*(4), 619–635. https://doi.org/10.1180/000985599546488

Winslow, M. A. (1983). Clastic dike swarms and the structural evolution of the foreland fold and thrust belt of the southern Andes. *Geological Society of America Bulletin*, *94*(9), 1073–1080. https://doi.org/10.1130/0016-7606(1983)94<1073:cdsats>2.0.co;2

Wirth, K. R., Naiman, Z. J., & Vervoort, J. D. (1997). The Chengwatana Volcanics, Wisconsin and Minnesota: Petrogenesis of the southernmost volcanic rocks exposed in the Midcontinent rift [Dataset]. *Canadian Journal of Earth Sciences*, *34*(4), 536–548. https://doi.org/10.1139/e17-043

Worden, R. H. & Morad, S. (Eds.) (2009). *Clay mineral cement in sandstones* (p. 520). John Wiley & Sons.

Wright, H. E. (1973). Tunnel valleys, glacial surges, and subglacial hydrology of the Superior Lobe. In R. F. Minnesota, R. F. Black, R. B. Goldthwait, & H. B. Willman (Eds.), *The Wisconsinan Stage, Geological Society of America Memoirs* (pp. 251–276). Geological Society of America.

Zartman, R. E., Nicholson, S. W., Cannon, W. F., & Morey, G. (1997). U–Th–Pb zircon ages of some Keweenawan Supergroup rocks from the south shore of Lake Superior. *Canadian Journal of Earth Sciences*, *34*(4), 549–561. https://doi.org/10.1139/e17-044

Zhang, Y., Hodgin, E. B., Alemu, T., Pierce, J., Fuentes, A., & Swanson-Hysell, N. L. (2024). Tracking Rodinia into the Neoproterozoic: New paleomagnetic constraints from the Jacobsville Formation. *Tectonics*, *43*(2), e2023TC007866. https://doi.org/10.1029/TC007866

Zhu, J., Poulsen, C. J., & Tierney, J. E. (2019). Simulation of Eocene extreme warmth and high climate sensitivity through cloud feedbacks. *Science Advances*, *5*(9), eaax1874. https://doi.org/10.1126/sciadv.aax1874

Ziegler, P. A., Cloetingh, S., & van Wees, J. D. (1995). Dynamics of intra-plate compressional deformation: The Alpine foreland and other examples. *Tectonophysics*, *252*(1–4), 7–59. https://doi.org/10.1016/0040-1951(95)00102-6

References From the Supporting Information

Anderson, N. T., Kelson, J. R., Kele, S., Daëron, M., Bonifacie, M., Horita, J., et al. (2021). A unified clumped isotope thermometer calibration (0.5–1,100°C) using carbonate-based standardization. *Geophysical Research Letters*, *48*(7), e2020GL092069. https://doi.org/10.1029/2020gl092069

Ballato, P., Nowaczyk, N. R., Landgraf, A., Strecker, M. R., Friedrich, A., & Tabatabaei, S. H. (2008). Tectonic control on sedimentary facies pattern and sediment accumulation rates in the Miocene foreland basin of the southern Alborz Mountains, Northern Iran. *Tectonics*, *27*(6), TC6001. https://doi.org/10.1029/2008tc002278

Bernasconi, S. M., Daëron, M., Bergmann, K. D., Bonifacie, M., Meckler, A. N., Affek, H. P., et al. (2021). InterCarb: A community effort to improve inter-laboratory standardization of the carbonate clumped isotope thermometer using carbonate standards. *Geochemistry, Geophysics, Geosystems*, *n/a*(5), e2020GC009588. https://doi.org/10.1029/2020gc009588

Bjørlykke, K. (1988). Sandstone diagenesis in relation to preservation, destruction and creation of porosity. In *Developments in sedimentology* (Vol. 41, pp. 555–588).

Bragov, A. M., Balandin, V. V., Igumnov, L. A., Kotov, V. L., Kruszka, L., & Lomunov, A. K. (2018). Impact and penetration of cylindrical bodies into dry and water-saturated sand. *International Journal of Impact Engineering*, *122*, 197–208. https://doi.org/10.1016/j.ijimpeng.2018.08.012

Brand, W. A., Assonov, S. S., & Coplen, T. B. (2010). Correction for the ^{17}O interference in $\delta(^{13}C)$ measurements when analyzing CO_2 with stable isotope mass spectrometry (IUPAC Technical Report). *Pure and Applied Chemistry*, *82*(8), 1719–1733. https://doi.org/10.1351/pac-rep-09-01-05

Burbank, D. W., Beck, R. A., Raynolds, R. G. H., Hobbs, R., & Tahirkheli, R. A. K. (1988). Thrusting and gravel progradation in foreland basins: A test of post-thrusting gravel dispersal. *Geology*, *16*(12), 1143–1146. https://doi.org/10.1130/0091-7613(1988)016<1143:tagpif>2.3.co;2

Cannon, W. F., Green, A. G., Hutchinson, D. R., Lee, M., Milkereit, B., Behrendt, J. C., et al. (1989). The North American Midcontinent Rift beneath Lake Superior from GLIMPCE seismic reflection profiling. *Tectonics*, *8*(2), 305–332. https://doi.org/10.1029/tc008i002p00305

Chamley, H. (1989). *Clay sedimentology*. Springer-Verlag.

Covey, A. K., Braun, S. A., Gualda, G. A., Bream, B. R., Fisher, C., Wooden, J. L., & Schmitz, M. D. (2012). Zirconia (NC) zircon as a potential standard. In *American Geophysical Union fall meeting abstracts* (Vol. 2012, p. V23C-2825).

Crowley, J. L., Schoene, B., & Bowring, S. A. (2007). U-Pb dating of zircon in the Bishop Tuff at the millennial scale. *Geology*, *35*(12), 1123–1126. https://doi.org/10.1130/g24017a.1

DeCelles, P. G., & Currie, B. S. (1996). Long-term sediment accumulation in the Middle Jurassic–early Eocene Cordilleran retroarc foreland-basin system. *Geology*, *24*(7), 591–594. https://doi.org/10.1130/0091-7613(1996)024<0591:ltsait>2.3.co;2

Dennis, K. J., Affek, H. P., Passey, B. H., Schrag, D. P., & Eiler, J. M. (2011). Defining an absolute reference frame for 'clumped' isotope studies of CO_2. *Geochimica et Cosmochimica Acta*, *75*(22), 7117–7131. https://doi.org/10.1016/j.gca.2011.09.025

Duffin, M. E. (1989). Nature and origin of authigenic K-feldspar in Precambrian basement rocks of the North American midcontinent. *Geology*, *17*(8), 765–768. https://doi.org/10.1130/0091-7613(1989)017<0765:naooak>2.3.co;2

Edmonsond, S., Nadeau, M. D., Turner, A. C., Wu, Z., Geyman, E. C., Ahm, A. S. C., et al. (2024). Shallow carbonate geochemistry in the Bahamas since the last interglacial period. *Earth and Planetary Science Letters*, *627*, 118566. https://doi.org/10.1016/j.epsl.2023.118566

Eiler, J. M., & Schauble, E. (2004). $^{18}O^{13}C^{16}O$ in Earth's atmosphere. *Geochimica et Cosmochimica Acta*, *68*(23), 4767–4777. https://doi.org/10.1016/j.gca.2004.05.035

Eyles, N. (2008). Glacio-epochs and the supercontinent cycle after~ 3.0 Ga: Tectonic boundary conditions for glaciation. *Palaeogeography, Palaeoclimatology, Palaeoecology*, *258*(1–2), 89–129. https://doi.org/10.1016/j.palaeo.2007.09.021

Fiebig, J., Bajnai, D., Löffler, N., Methner, K., Krsnik, E., Mulch, A., & Hofmann, S. (2019). Combined high-precision Δ48 and Δ47 analysis of carbonates. *Chemical Geology*, *522*, 186–191. https://doi.org/10.1016/j.chemgeo.2019.05.019

Friend, P. F. (1978). Distinctive features of some ancient river systems. In A. D. Miall (Ed.), *Fluvial sedimentology*, *Can. Soc. Petrol. Geol. Mem.* (Vol. 5, pp. 531–542).

Gagnon, C. A., Butler, K. L., Gaviria, E., Terrazas, A., Gao, A., Bhattacharya, T., et al. (2023). Paleoclimate controls on lithium enrichment in Great Basin Pliocene–Pleistocene lacustrine clays. *Bulletin*, *135*(11–12), 3201–3212. https://doi.org/10.1130/B36572.1

Gerstenberger, H., & Haase, G. (1997). A highly effective emitter substance for mass spectrometric Pb isotope ratio determinations. *Chemical Geology*, *136*(3–4), 309–312. https://doi.org/10.1016/S0009-2541(96)00033-2

Geyman, E. C., Wu, Z., Nadeau, M. D., Edmonsond, S., Turner, A., Purkis, S. J., et al. (2022). The origin of carbonate mud and implications for global climate. *Proceedings of the National Academy of Sciences*, *119*(43), e2210617119. https://doi.org/10.1073/pnas.2210617119

Hampton, B. A., & Horton, B. K. (2007). Sheetflow fluvial processes in a rapidly subsiding basin, Altiplano plateau, Bolivia. *Sedimentology*, *54*(5), 1121–1148. https://doi.org/10.1111/j.1365-3091.2007.00875.x

Hiess, J., Condon, D. J., McLean, N., & Noble, S. R. (2012). $^{238}U/^{235}U$ systematics in terrestrial uranium-bearing minerals. *Science*, *335*(6076), 1610–1614. https://doi.org/10.1126/science.1215507

Hill, C. A., Polyak, V. J., Asmerom, Y., & P. Provencio, P. C. T. C. (2016). Constraints on a Late Cretaceous uplift, denudation, and incision of the Grand Canyon region, southwestern Colorado Plateau, USA, from U-Pb dating of lacustrine limestone. *Tectonics*, *35*(4), 896–906. https://doi.org/10.1002/2016tc004166

Huntington, K. W., Eiler, J. M., Affek, H. P., Guo, W., Bonifacie, M., Yeung, L. Y., et al. (2009). Methods and limitations of 'clumped' CO_2 isotope (Δ_{47}) analysis by gas-source isotope ratio mass spectrometry. *Journal of Mass Spectrometry*, *44*(9), 1318–1329. https://doi.org/10.1002/jms.1614

Ibarra, D. E., Yanchilina, A. G., Lloyd, M. K., Methner, K. A., Chamberlain, C. P., Yam, R., et al. (2022). Triple oxygen isotope systematics of diagenetic recrystallization of diatom opal-A to opal-CT to microquartz in deep sea sediments. *Geochimica et Cosmochimica Acta*, *320*, 304–323. https://doi.org/10.1016/j.gca.2021.11.027

Jackson, S. E., Pearson, N. J., Griffin, W. L., & Belousova, E. A. (2004). The application of laser ablation-inductively coupled plasma-mass spectrometry to in situ U-Pb zircon geochronology. *Chemical Geology*, *211*(1–2), 47–69. https://doi.org/10.1016/j.chemgeo.2004.06.017

Kaushik, A., Gupta, A. K., Clemens, S. C., Kumar, P., Sanyal, P., Gupta, P., et al. (2023). Paleoclimatic reconstruction of northwest Himalaya since CE 475 using lake sediments from Tadag Taal, Kumaun, India. *Palaeogeography, Palaeoclimatology, Palaeoecology*, *619*, 111544. https://doi.org/10.1016/j.palaeo.2023.111544

Krogh, T. E. (1973). A low-contamination method for hydrothermal decomposition of zircon and extraction of U and Pb for isotopic age determinations. *Geochimica et Cosmochimica Acta*, *37*(3), 485–494. https://doi.org/10.1016/0016-7037(73)90213-5

Kuiper, Y. D., Murray, D. P., Ellison, S., & Crowley, J. L. (2022). U-Pb detrital zircon analysis of sedimentary rocks of the southeastern New England Avalon terrane in the U.S. Appalachians: Evidence for a separate crustal block. In Y. D. Kuiper, J. B. Murphy, R. D. Nance, R. A. Strachan, & M. D. Thompson (Eds.), *New developments in the Appalachian-Caledonian-Variscan Orogen*. Geological Society of America.

Kylander-Clark, A. R. (2020). Expanding the limits of laser-ablation U–Pb calcite geochronology. *Geochronology*, *2*(2), 343–354. https://doi.org/10.5194/gchron-2-343-2020

Kylander-Clark, A. R. C., Hacker, B. R., & Cottle, J. M. (2013). Laser-ablation split-stream ICP petrochronology. *Chemical Geology*, *345*, 99–112. https://doi.org/10.1016/j.chemgeo.2013.02.019

Lloyd, M. K., Ryb, U., & Eiler, J. M. (2018). Experimental calibration of clumped isotope reordering in dolomite. *Geochimica et Cosmochimica Acta*, *242*, 1–20. https://doi.org/10.1016/j.gca.2018.08.036

Macdonald, F. A., Yonkee, W. A., Flowers, R. M., & Swanson-Hysell, N. L. (2023). Neoproterozoic of Laurentia. https://doi.org/10.1130/2022.1220(19)

Mattinson, J. M. (2005). Zircon U-Pb chemical abrasion ("CA-TIMS") method: Combined annealing and multi-step partial dissolution analysis for improved precision and accuracy of zircon ages. *Chemical Geology*, *220*(1–2), 47–66. https://doi.org/10.1016/j.chemgeo.2005.03.011

Mueller, S. A. (2021). Structural analysis and interpretation of deformation along the Keweenaw fault system west of Lake Gratiot, Keweenaw County, Michigan [Master's thesis]. Michigan Technological University. https://doi.org/10.37099/mtu.dc.etdr/1167

Nuriel, P., Wotzlaw, J.-F., Stremtan, C., Vaks, A., & Kylander-Clark, A. R. (2020). The use of ASH15 flowstone as matrix-matched standard for laser-ablation geochronology of calcite. *Geochronology Discussions*, *2020*, 1–26. https://doi.org/10.5194/gchron-2020-22

Odin, G., Montanari, A., Deino, A., Drake, R., Guise, P., Kreuzer, H., & Rex, D. (1991). Reliability of volcano-sedimentary biotite ages across the Eocene-Oligocene boundary (Apennines, Italy). *Chemical Geology*, *86*(3), 203–224. https://doi.org/10.1016/0168-9622(91)90050-7

Passey, B. H., Levin, N. E., Cerling, T. E., Brown, F. H., & Eiler, J. M. (2010). High-temperature environments of human evolution in East Africa based on bond ordering in paleosol carbonates. *Proceedings of the National Academy of Sciences*, *107*(25), 11245–11249. https://doi.org/10.1073/pnas.1001824107

Paton, C., Woodhead, J. D., Hellstrom, J. C., Hergt, J. M., Greig, A., & Maas, R. (2010). Improved laser ablation U-Pb zircon geochronology through robust downhole fractionation correction. *Geochemistry, Geophysics, Geosystems*, *11*(3), 1–36. https://doi.org/10.1029/2009GC002618

Roberts, N. M. W., Rasbury, E. T., Parrish, R. R., Smith, C. J., Horstwood, M. S. A., & Condon, D. J. (2017). A calcite reference material for LA-ICP-MS U-Pb geochronology. *Geochemistry, Geophysics, Geosystems*, *18*(7), 2807–2814. https://doi.org/10.1002/2016GC006784

Schmitz, M. D., & Schoene, B. (2007). Derivation of isotope ratios, errors, and error correlations for U-Pb geochronology using ^{205}Pb-^{235}U-(^{233}U)-spiked isotope dilution thermal ionization mass spectrometric data. *Geochemistry, Geophysics, Geosystems*, *8*(8), 1–20. https://doi.org/10.1029/2006GC001492

Schoene, B., Crowley, J. L., Condon, D. J., Schmitz, M. D., & Bowring, S. A. (2006). Reassessing the uranium decay constants for geochronology using ID-TIMS U–Pb data. *Geochimica et Cosmochimica Acta*, *70*(2), 426–445. https://doi.org/10.1016/j.gca.2005.09.007

Sharp, Z. D. (1990). A laser-based microanalytical method for the in situ determination of oxygen isotope ratios of silicates and oxides. *Geochimica et Cosmochimica Acta*, *54*(5), 1353–1357. https://doi.org/10.1016/0016-7037(90)90160-m

Sharp, Z. D., & Wostbrock, J. A. (2021). Standardization for the triple oxygen isotope system: Waters, silicates, carbonates, air, and sulfates. *Reviews in Mineralogy and Geochemistry*, *86*(1), 179–196. https://doi.org/10.2138/rmg.2021.86.05

Sharp, Z. D., Wostbrock, J. A. G., & Pack, A. (2018). Mass-dependent triple oxygen isotope variations in terrestrial materials. *Geochemical Perspectives Letters*, *7*, 27–31. https://doi.org/10.7185/geochemlet.1815

Sláma, J., Košler, J., Condon, D. J., Crowley, J. L., Gerdes, A., Hanchar, J. M., et al. (2008). Plešovice zircon - A new natural reference material for U-Pb and Hf isotopic microanalysis. *Chemical Geology*, *249*(1–2), 1–35. https://doi.org/10.1016/j.chemgeo.2007.11.005

Środoń, J. (1984). Mixed-layer illite-smectite in low-temperature diagenesis: Data from the Miocene of the Carpathian foredeep. *Clay Minerals*, *19*(2), 205–215. https://doi.org/10.1180/claymin.1984.019.2.07

Stein, C. A., Kley, J., Stein, S., Hindle, D., & Keller, G. R. (2015). North America's Midcontinent Rift: When rift met LIP. *Geosphere*, *11*(5), 1607–1616. https://doi.org/10.1130/GES01183.1

Stein, R. A., Turner, A. C., Amundson, R., & Stolper, D. A. (2023). Clumped isotope thermometry in plant-derived carbonates. *Paleoceanography and Paleoclimatology*, *38*(3), e2022PA004473. https://doi.org/10.1029/2022PA004473

Swart, P. K., Burns, S. J., & Leder, J. J. (1991). Fractionation of the stable isotopes of oxygen and carbon in carbon dioxide during the reaction of calcite with phosphoric acid as a function of temperature and technique. *Chemical Geology: Isotope Geoscience Section*, *86*(2), 89–96. https://doi.org/10.1016/0168-9622(91)90055-2

Tesauro, M., Kaban, M. K., & Mooney, W. D. (2015). Variations of the lithospheric strength and elastic thickness in North America. *Geochemistry, Geophysics, Geosystems*, *16*(7), 2197–2220. https://doi.org/10.1002/2015gc005937

Tyrrell, C. (2019). Keweenaw fault geometry and slip kinematics-Bête Grise Bay, Keweenaw Peninsula, Michigan [Master's thesis]. Michigan Technological University. https://doi.org/10.37099/mtu.dc.etdr/947

Van Horn, J. E. (1980). Seismotectonic study of the southwestern Lake Superior region utilizing the upper Michigan northern Wisconsin seismic network [M.S. thesis]. Michigan Technological University.

Watkins, J. M., Hunt, J. D., Ryerson, F. J., & DePaolo, D. J. (2014). The influence of temperature, pH, and growth rate on the $\delta^{18}O$ composition of inorganically precipitated calcite. *Earth and Planetary Science Letters*, *404*, 332–343. https://doi.org/10.1016/j.epsl.2014.07.036

Watson, E. B., Wark, D. A., & Thomas, J. B. (2006). Crystallization thermometers for zircon and rutile. *Contributions to Mineralogy and Petrology*, *151*(4), 413–433. https://doi.org/10.1007/s00410-006-0068-5

Wiedenbeck, M., Allé, P., Corfu, F., Griffin, W. L., Meier, F., Oberli, F., et al. (1995). Three natural zircon standards for U-Th-Pb, Lu-Hf, trace element and REE analyses. *Geostandards Newsletter*, *19*, 1–23. https://doi.org/10.1111/j.1751-908x.1995.tb00147.x

Wilkinson, M., Haszeldine, R. S., Morton, A., & Fallick, A. E. (2014). Deep burial dissolution of K-feldspars in a fluvial sandstone, Pentland Formation, UK Central North Sea. *Journal of the Geological Society*, *171*(5), 635–647. https://doi.org/10.1144/jgs2013-144

Worden, R. H., & Morad, S. (1999). Clay minerals in sandstones: Controls on formation, distribution and evolution. In *Clay mineral cements in sandstones* (pp. 1–41).

Wostbrock, J. A., Cano, E. J., & Sharp, Z. D. (2020). An internally consistent triple oxygen isotope calibration of standards for silicates, carbonates and air relative to VSMOW2 and SLAP2. *Chemical Geology*, *533*, 119432. https://doi.org/10.1016/j.chemgeo.2019.119432

Wostbrock, J. A., & Sharp, Z. D. (2021). Triple oxygen isotopes in silica–water and carbonate–water systems. *Reviews in Mineralogy and Geochemistry*, *86*(1), 367–400. https://doi.org/10.2138/rmg.2021.86.11

Young, C. T., & Repasky, T. R. (1986). A magnetotelluric transect of the Jacobsville Sandstone in northern Michigan. *Geological Society of America Bulletin*, *97*(6), 711–716. https://doi.org/10.1130/0016-7606(1986)97<711:amtotj>2.0.co;2

Erratum

The originally published version of this article contained a typographical error. The Douglas Fault was incorrectly abbreviated throughout as “DF.” The error has been corrected, and this may be considered the authoritative version of record.